

1 *Research article*

2 **Automated riverbed composition analysis using Deep Learning** 3 **on underwater images**

4 Alexander A. Ermilov¹, Gergely Benkő¹ and Sándor Baranya¹

5 ¹Department of Hydraulic and Water Resources Engineering, Budapest University of Technology and Economics,
6 Budapest, 1111, Hungary

7 *Correspondence to:* Alexander A. Ermilov (ermilov.alexander@emk.bme.hu)

8 **Abstract.** The sediment of alluvial riverbeds plays a significant role in river systems both in engineering and
9 natural processes. However, the sediment composition can show ~~high-great~~ spatial and temporal heterogeneity,
10 even on river reach scale, making it difficult to representatively sample and assess. ~~Conventional sampling~~
11 ~~methods are inadequate and time-consuming for effectively capturing the variability of bed surface texture in~~
12 ~~these situations~~ ~~Conventional sampling methods in such cases cannot describe well the variability of the bed~~
13 ~~surface texture due to the amount of energy and time they would require.~~ ~~In this study, we overcome this issue by~~
14 ~~adopting an image-based, Deep Learning (DL) algorithm~~ ~~In this manuscript, an attempt is made to overcome this~~
15 ~~issue by introducing a novel image-based, Deep Learning (DL) algorithm and related field measurement~~
16 ~~methodology with potential for becoming a complementary technique for bed material samplings and significantly~~
17 ~~reducing the necessary resources.~~ The algorithm was trained to recognise main sediment classes in videos ~~that~~
18 ~~were taken along cross-sections underwater in the Danube river.~~ ~~27 river bed samples were collected and analyzed~~
19 ~~for validation.~~ ~~that were taken underwater in a large river with mixed bed sediments, along cross sections, using~~
20 ~~In total, 27 physical bedmaterial samples were collected and sieved for the validation purposes.~~ The introduced
21 DL-based method is fast, i.e., the videos of 300-400-meter-long sections can be analysed within minutes, with
22 ~~continuous-very dense~~ spatial sampling distribution (i.e., the whole riverbed along the path is mapped with images,
23 in cca. 0.3 – 1 m² sized, overlapping windows). The ~~quality-goodness~~ of the trained algorithm was evaluated i)
24 mathematically by dividing the annotated images into test and validation sets, and also via ii) intercomparison
25 with other direct (sieving of physical samples) and indirect sampling methods (wavelet-based image processing
26 of the riverbed images), focusing on the percentages of the detected sediment fractions. For the final evaluation,
27 the sieving analysis of the collected physical samples were considered as the ground truth. ~~This meant a total of~~
28 ~~27 measurement points, where the DL results could be compared with the two other methods.~~ ~~After correcting for~~
29 ~~samples affected by bed armouring, comparison of the DL approach with 14 physical samples yielded a mean~~
30 ~~classification error of 4.5%.~~ ~~During data processing, outlier points, where the collected physical samples did not~~
31 ~~represent the riverbed surface images taken there (e.g., due to bedarmour), were removed.~~ ~~In the remaining 14~~
32 ~~points, the DL algorithm produced promising results with a mean error of 4.5%.~~ Besides, the spatial trend in the
33 fraction changes was also well captured along the cross-sections, based upon the visual evaluation of the footages.
34 ~~Furthermore, comparison with the wavelet based image processing justified the selection of the outlier points~~
35 ~~earlier, as its results matched closely with the DL detections in these purely gravel covered points and showed no~~
36 ~~sign of finer fractions, univocally opposing the content of the physical samples.~~ Suggestions for performing proper
37 field measurements are also given, furthermore, possibilities for combining the algorithm with other techniques
38 are highlighted, briefly showcasing the multi-purpose of underwater videos for hydromorphological assessment.

39 **Keywords:** riverbed texture, underwater mapping, sediment classes, Artificial Intelligence, Deep Learning,
40 image-based

41 **1 Introduction**

42 The physical composition of a riverbed plays a crucial role in fluvial hydromorphological processes, as a sort of
43 boundary condition in the interaction mechanisms between the flow and the solid bed. Within these processes, the
44 grains on the riverbed are responsible for multiple phenomena, such as flow resistance (Vanoni and Hwang, 1967;
45 Zhou et al., 2021), stability of the riverbed (Staudt et al., 2018; Obodovskyi et al., 2020), development of bed
46 armour (Rákóczi, 1987; Ferdowski et al., 2017), sediment clogging (Rákóczi, 1997; Fetzer et al., 2017), fish shelter
47 (Scheder et al., 2015), etc. Through these physical processes, the bed material composition has a determining
48 effect on numerous river-uses, e.g., possibilities of inland waterway transport (Xiao et al., 2021), drinking water
49 supply through bank filtration (Cui et al., 2021), or the quality of riverine habitats (Muñoz-Mas et al., 2019)..
50 Knowledge of riverbed morphology and sediment composition (sand, gravel and cobble content) is therefore of
51 major importance in river hydromorphology. In order to gain information about riverbed sediments, in situ field
52 sampling methodologies are implemented.

53
54 Traditionally, bed material sampling methods are intrusive (i.e., sediment is physically extracted from the bed for
55 follow-up analysis) and carried out via collecting the sediment grains one-by-one (areal, grid-by-number and
56 pebble count methods, see e.g., Bunte and Abt, 2001; Guerit et al., 2018) or in a larger amount by a variety of
57 grab samplers (volumetric methods, such as WMO, 1981; Singer, 2008). This is then followed by measuring their
58 sizes individually on-site or transporting them to a laboratory for mass-sieving analysis (Fehr, 1987; Diplas, 1988;
59 Bunte and Abt, 2001). These sampling procedures are time- and energy consuming, especially in large gravel and
60 mixed bed rivers, where characteristic grain sizes can strongly vary both in time and space (Wolcott and Church,
61 1991; USDA, 2007), requiring a dense sampling point allocation. The same goes for critical river reaches, where
62 significant human impact led to severe changes in the morphological state of the rivers (e.g., the Upper section of
63 the Hungarian Danube; Török and Baranya, 2017). When assessing bed material composition on a river reach
64 scale, experts usually try to extrapolate from the samples, and describe larger regions of the bed (even several
65 thousand m²) by data gathered in a few, several dozen points (see e.g., USDA, 2007; Haddadchi et al., 2018;
66 Baranya et al., 2018; Sun et al., 2021). Gaining a representative amount of the sediment samples is also a critical
67 issue. For instance, following statistical criteria such as those of Kellerhals and Bray (1971) or Adams (1979), a
68 representative sample should weigh ten-to-hundred kg. Additionally, physical bed material sampling methods are
69 unable to directly quantify important, hydromorphological features such as roughness or bedforms (Graham et al.,
70 2005). Due to these constraints, surrogate approaches have recently been **intensively** tested to analyse the riverbed.
71 **Major eE**xamples are introduced in the rest of this section. Unlike the conventional methods, these techniques are
72 non-intrusive and rely on computers and other instrumentation to decrease the need of human intervention and
73 speed up the analyses.

74
75 One group of the surrogate approaches is the acoustic methods, where an acoustic wave source (e.g., an Acoustic
76 Doppler Current Profiler; ADCP) is pointed towards the riverbed from a moving vessel, emitting a signal. The
77 strength and frequency of this signal is measured while it passes through the water column, reflecting back to the

78 receiver from the sediment transported by the river, and finally from the riverbed itself. This approach is fast and
79 larger areas can be covered relatively quickly (Grams et al., 2013). While it has already become widely used for
80 describing sediment movement (i.e., suspended sediment, Guerrero et al., 2016; bedload, Muste et al., 2016; and
81 indirectly flow velocity; Shields and Rigby, 2005) and channel shape (Zhang et al., 2008), it has not reached
82 similar breakthrough for riverbed material analysis. Researchers experimented with the reflecting signal strength
83 [dB] from the riverbed (e.g., Shields, 2010) to establish its relationship with the riverbed material. Their hypothesis
84 was that the absorption (and hence the reflectance) of the acoustic waves reaching the bed correlates with the type
85 of bed sediment. Following initial successes, the method presented several disadvantages and limitations, hence
86 it could not establish itself as surrogate method for riverbed material measurements so far. For example, Shields
87 (2010) showed that it was necessary to apply instrument specific coefficients to convert the signal strength into
88 bed hardness, and these coefficients could only be derived by first validating each instrument using collected
89 sediment samples with corresponding ADCP data. Moreover, the method was sensitive to the bulk density of the
90 sediment and to bedforms. Based on his results and observations, the sediment classification could only extend to
91 differentiate between cohesive (clay, silt) and non-cohesive (sand, gravel) sediment patches, but gravel could not
92 be distinguished strongly from sand as they produced similar backscatter strengths. Buscombe et al. (2014a;
93 2014b) further elaborated on the topic and successfully developed a better, less limited, decision tree-based
94 approach. They showed that spectral analysis of the backscatter is much more effective for differentiating the
95 sediment types compared to the statistical analysis used by Shields. With this approach it became possible to
96 classify homogenous sand, gravel, and cobble patches. However, Buscombe et al. (2014a, 2014b) also emphasizes
97 that acoustic approaches are not capable of separating the effects of surface roughness from the effects of
98 bedforms, therefore the selection of an appropriate ensemble averaging window size is of great importance for
99 their introduced method. This size has to be small enough to not include morphological signal, for which however,
100 the a priori analyses of riverbed elevation profiles is needed at each site. Furthermore, they suggest their method
101 is sensitive to and limited by high concentrations of (especially cohesive) sediment, therefore its application to
102 heterogeneous riverbeds would require site specific calibrations. The above-mentioned studies also note that
103 acoustic methods in general inherently do not allow the measurement of individual sediment grains due to their
104 spatial averaging nature. The detected signal strength correlates with the median grainsize of the covered area,
105 information about other nominal grain sizes cannot be gained.

106
107 Another group of the surrogate approaches is the application of photography (Adams, 1979; Ibbekken and
108 Schleyer, 1986) and later computer vision or image-processing techniques. During the last two decades, two major
109 subgroups emerged: one uses object- and edge detection (by finding abrupt changes in intensity and brightness of
110 the image, segmenting objects from each other; Sime and Ferguson, 2003; Detert and Weitbrecht, 2013), and the
111 other one analyses the textural properties of the whole image, using autocorrelation and semi-variance methods
112 to define empirical relationship between image texture and the grain sizes of the photographed sediments (Rubin,
113 2004; Verdú et al., 2005). Both image processing approaches were very time consuming and required mostly site-
114 specific manual settings, however, a few transferable and more automated techniques have also been developed
115 recently (e.g., Graham et al., 2005; Buscombe, 2013). Even though there is a continuous improvement in the
116 applied image-based bed sediment analysis methods, there are still major limitations the users face with, such as:
117

- 118 • Most of the studies (all the ones listed above) focuses on gravel bed rivers, and only a few exceptions
119 can be found in the literature where sand is also accounted for (texture-based methods;e.g.:
120 Buscombe, 2013).
- 121 • The adaptation environment was typically non-submerged sediment, instead of underwater
122 conditions (a few exceptions: Chezar and Rubin, 2004; Warrick et al., 2009).
- 123 • The computational demand of the image processing is high (e.g., one to ten minutes per image;
124 Detert and Weitbrecht, 2013).
- 125 • The analysis requires operator expertise (higher than in case of any conventional method).
- 126 • There is an inherent pixel- and image resolution limit (Buscombe and Masselink, 2008 Cheng, 2015;
127 Purinton and Bookhagen, 2019). The finer the sediment, the higher resolution of the images is
128 required (higher calculation time), or they must be taken from a closer position (smaller area and
129 sample per image).

130

131 Nowadays, with the rising popularity of Artificial Intelligence (AI), several Machine Learning (ML) techniques
132 have been implemented in image recognition as well. The main approaches of segmentation contra textural
133 analysis still remain; however, an AI defines the empirical relationship between the object sizes (Igathinatane et
134 al., 2009; Kim et al., 2020) or texture types (Buscombe and Ritchie, 2018) in the images and their real sizes. In
135 the field of river sedimentology a few examples can already be found, where ML (e.g., Deep Learning; DL) was
136 implemented. For instance, Rozniak et al. (2019) developed an algorithm for gravel-bed rivers, performing
137 textural analysis. With this approach, information is not gained on individual grains (e.g., their individual shape
138 and position), but rather the general grain size distribution (GSD) of the whole images. At certain points of the
139 studied river basins, conventional physical samplings (pebble count) were performed to provide real GSD
140 information. Using this data, the algorithm was trained (with ~1000 images) to estimate GSD for the rest of the
141 study site, based on the images. The method worked for areas where grain diameters were larger than 5 mm, and
142 the sediment was well-sorted. The developed method showed sensitivity to sand coverage, blurs, reduced
143 illuminations (e.g., shadows) and white pixels. Soloy et al. (2020) presented an algorithm which used object
144 detection on gravel- and cobble covered beaches to calculate individual grain sizes and shapes. 46 images were
145 used for the model training, however, the number of images were multiplied with data augmentation (rotating,
146 cropping, blurring the images; see Perez and Wang, 2017) to enhance the learning session and increase the input
147 data. The method was able to reach a limited execution speed of a few seconds per m² and adequately measured
148 the sizes of gravels. Ren et al. (2020) applied an ensemble bagging-based Machine Learning (ML) algorithm to
149 estimate GSD along the 70 km long Hanford Reach of the Columbia River. Due to its economic importance, a
150 large amount of measurement data has been accumulated for this study site over the years, making it ideal for
151 using ML. By the time of the study, 13,372 scaled images (i.e., their millimetre/pixel ratio was known) were taken
152 both underwater and in the dry zones, covering approx. 1 m² area each. The distance between the image-sampling
153 points was generally between 50-70 m. An expert defined the GSD (8 sediment classes) of each image by using a
154 special, visual evaluation-classification methodology (Delong and Brusven, 1991; Geist et al., 2000). This dataset
155 was fed to a ML algorithm along with their corresponding bathymetric attributes and hydrodynamic properties,
156 simulated with a 2D hydrodynamic model. Then, it was tested to predict the sediment classes based on the
157 hydrodynamic parameters only. The algorithm performed with a mean accuracy of 53%. Even though this method

158 was not image-based (only indirectly, via the origin of the GSD data), it highlighted the possibilities of an AI for
159 a predictive model, using a high-dimensional dataset. Having such a large data of grain size information can be
160 considered exceptional and takes a huge amount of time to gather, even with the visual classification approach
161 they adapted. Moreover, this was still considered spatially sparse information (point-like measurements, 1 m²
162 covered area/image dozens of meters away from each other). Buscombe (2020) used a set of 400 scaled images
163 to train an AI algorithm on image texture properties, using another image-processing method (Barnard et al., 2007)
164 for validation. The algorithm reached a good result for not only gravel, but sand GSD calculation as well,
165 outperforming an earlier, but promising, texture-based method (wavelet analysis; Buscombe, 2013). In addition,
166 the method required fewer calibration parameters than the wavelet image-processing approach. The study also
167 foresaw the possibility to train an AI which estimates the real sizes of the grains, without knowing the scale of
168 one pixel (mm/pixel ratio) if the training is done properly. The AI might learn unknown relationships between the
169 texture and sizes if it is provided with a wide variety (images of several sediment classes) and scale (mm/pixel
170 ratio)) of dataset (however, it is also prone to learn unwanted biases). Recently, Takechi et al. (2021) further
171 elaborated on the importance of shadow- detection and removal, using a dataset of 500 pictures for training a
172 texture-based AI, with the help of an object-detecting image-processing technique (Basegrain; Detert and
173 Weitbrecht, 2013). The previously presented studies, applying ML and DL techniques, significantly contributed
174 to the development and improvement of surrogate sampling methods, incorporating the great potential in AI.
175 However, there are still several shortcomings to these procedures. Firstly, none of the image-based AI studies
176 used underwater recordings, even though the underwater environment offers completely different challenges.
177 Secondly, the training images were always scaled, i.e., the sizes of the grains could be easily reconstructed, which
178 is again complicated to accomplish in a river. Lastly, they were not adapted for continuous (i.e., spatially dense)
179 measurement, but rather focused on a sparse grid-like approach.

180
181 The goal of this ~~study-manuscript~~ is to further investigate the applicability of image processing as a surrogate
182 method, and attempt ~~solve the to break through or go around the above mentioned~~ shortcomings of ~~previous-the~~
183 AI-based approaches. Hence, we introduce a riverbed material analysing, ~~Deep Learning (DL)~~ algorithm and field
184 measurement methodology, along with our first set of results. The introduced technique can be used to measure
185 the gravel and sand content of the submerged riverbed surface. It aims to eventually become a practical tool for
186 exploratory mapping, by detecting sedimentation features (e.g., deposition zones of fine sediment, colmation
187 zones, bed armour) and helping decision making for river sedimentation management. Also, the long-term
188 hypothesis of the authors includes the creation of an image-based measurement methodology, where underwater
189 videos of the riverbed could serve multiple sediment related purposes simultaneously. Part of which is the current
190 approach for mapping the riverbed material texture and composition. Others include measuring the surface
191 roughness of the bed (Ermilov et al., 2020) and detecting bedload movement (Ermilov et al., 2022).

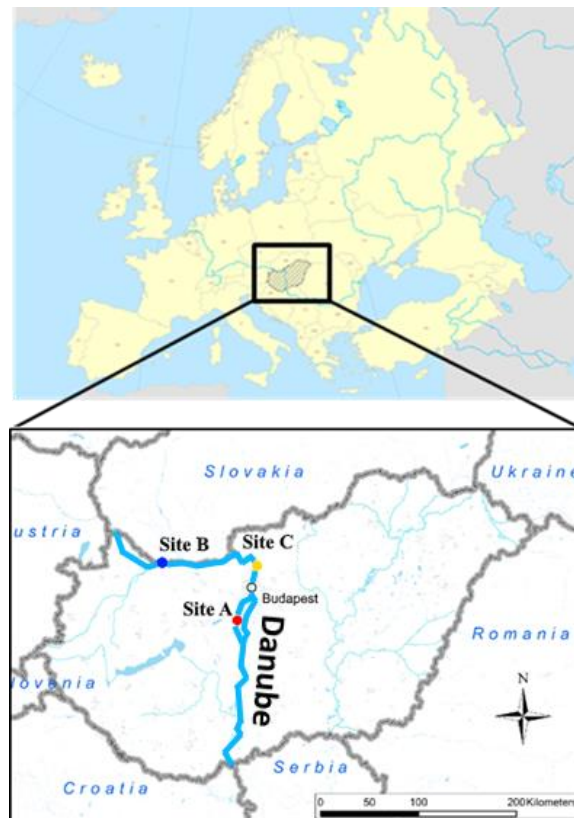
192
193 Compared to the studies introduced earlier, the main novelty of our ~~study-manuscript~~ is that both the training and
194 analysed videos are recorded underwater, continuously along cross-sections of a large river. Furthermore, the
195 training is unscaled, i.e., the camera-riverbed distance ~~varies-could vary~~ while recording the videos, without
196 considering image-scale. Moreover, compared to the relatively low number of training images in most ~~of the~~
197 ~~above-referred~~~~previous~~ studies, we used a very large dataset (~15000) of sediment images for the texture-based

198 AI, containing mostly sand, gravel, cobble, and to a smaller extent: bedrock together with some other, non-
199 sediment related objects.
200

201 2 Methods

202 2.1 Case studies

203 The results presented in this study are based on riverbed videos taken during three measurement campaigns, in
204 sections of the Danube River, Hungary. The first campaign was at Site A, Ercsi settlement (~ 1606 rkm) where 3
205 transects were recorded, the second one was at Site B, Gönyű settlement (~ 1791 rkm) with 2 transects, and the
206 third was at Site C, near to Göd settlement (~ 1667 rkm) with 2 transects (Fig. 1). Each transect was recorded
207 separately (one video per transect), therefore our dataset included a total of 8 videos.



208
209 **Figure 1: The location of the riverbed videos, where the underwater recordings took place. All sites were located in**
210 **Hungary, Central Europe. The surveys were carried out on the Danube River, Hungary's largest river.**

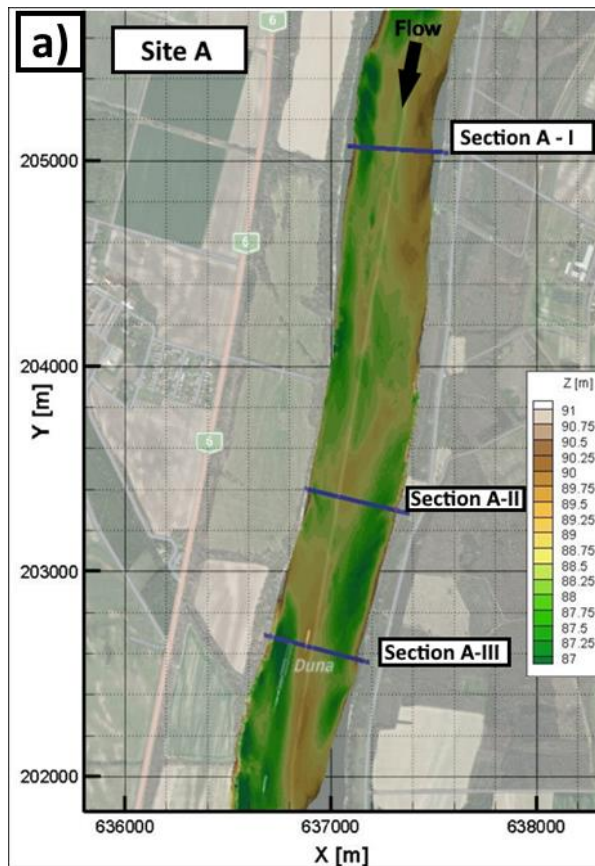
211 The training of the DL algorithm was done using the video images of Site C and a portion of A (test set; see later
212 in Section 2.3), while Site B and the rest of the images from A served for validation. The measurements were
213 carried out during daytime, at mid-water regime ($Q = 1900 \text{ m}^3/\text{s}$) in case of Site A, and low water regime ($Q =$
214 $1350 \text{ m}^3/\text{s}$) at Site B, and Site C ($Q = 700 \text{ m}^3/\text{s}$). This latter site served only for increasing the training image
215 dataset (i.e., conventional samplings were not carried out at the time of recording the videos), thus we do not go
216 into further details with it for the rest of the study-manuscript, but the main characteristics are listed in Table 1.

217

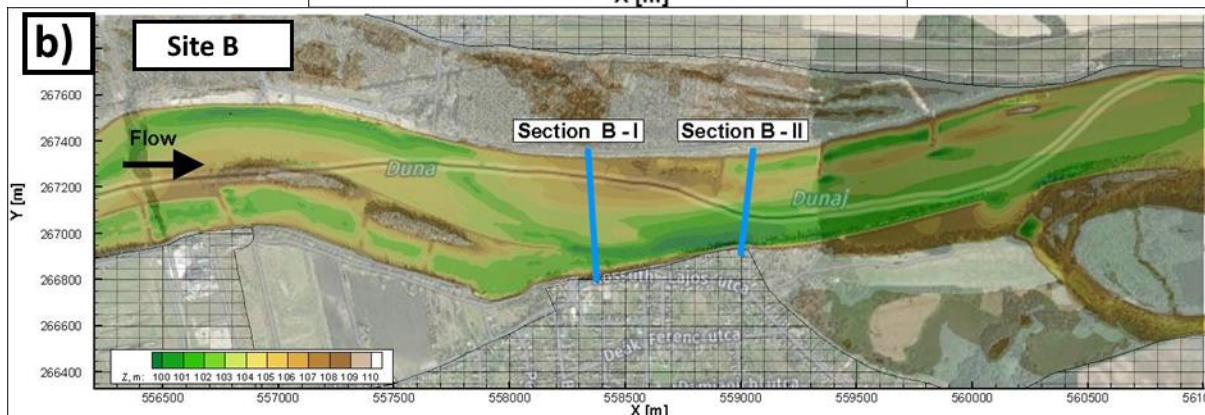
	Site A	Site B	Site C
Q_{survey} [m^3/s]	1900	1350	700
B_{survey} [m]	300 – 450		
$H_{\text{mean, survey}}$ [m]	3.5 - 4.5		
S_{survey} [cm/km]	15		
SSC_{survey} [mg/l]	25	20	14
Characteristic sediment riverbed	gravel, sandy gravel	gravel, gravelly sand	gravel, sandy gravel
$Q_{\text{annual, mean}}$ [m^3/s]	2000	2200	1400
$Q_{1\%}$ [m^3/s]	5300	5500	4700

218 **Table 1: Main hydromorphological parameters of the measurement sites. Q_{survey} : discharge during survey; B_{survey} : river**
219 **width during survey; $H_{\text{mean, survey}}$: mean water depth during the survey; S_{survey} : riverbed slope during survey; SSC_{survey} :**
220 **mean suspended sediment concentration during the survey; $Q_{\text{annual, mean}}$: annual-mean of the discharge at the site; $Q_{1\%}$:**
221 **flood with 1% annual exceedance probability.**

222 As underwater visibility conditions are influenced by the suspended sediment (SSC_{survey} – susp. sed.
223 concentration), the characteristics of this sediment transport is also included in Table 1. The highest water depths
224 were around 6-7 m in all cases. In Site A, measurements included mapping of the riverbed with a camera along
225 three separate transects (Fig. 2a). At Site B, two transects were recorded (Fig. 2b).



226



227

228

229

230

231

Figure 2: Bathymetry of Site A and B The measurement cross-sections are also marked. The vessel moved along these lines from one bank to the other, while carrying out ADCP measurement and recording riverbed videos. Physical bed material samples were also collected in certain points of these sections. The X and Y coordinates are given in EOVS, which refers to the Hungarian Uniform National Projection system,

232

233 2.2 Field data collection

234

235

236

237

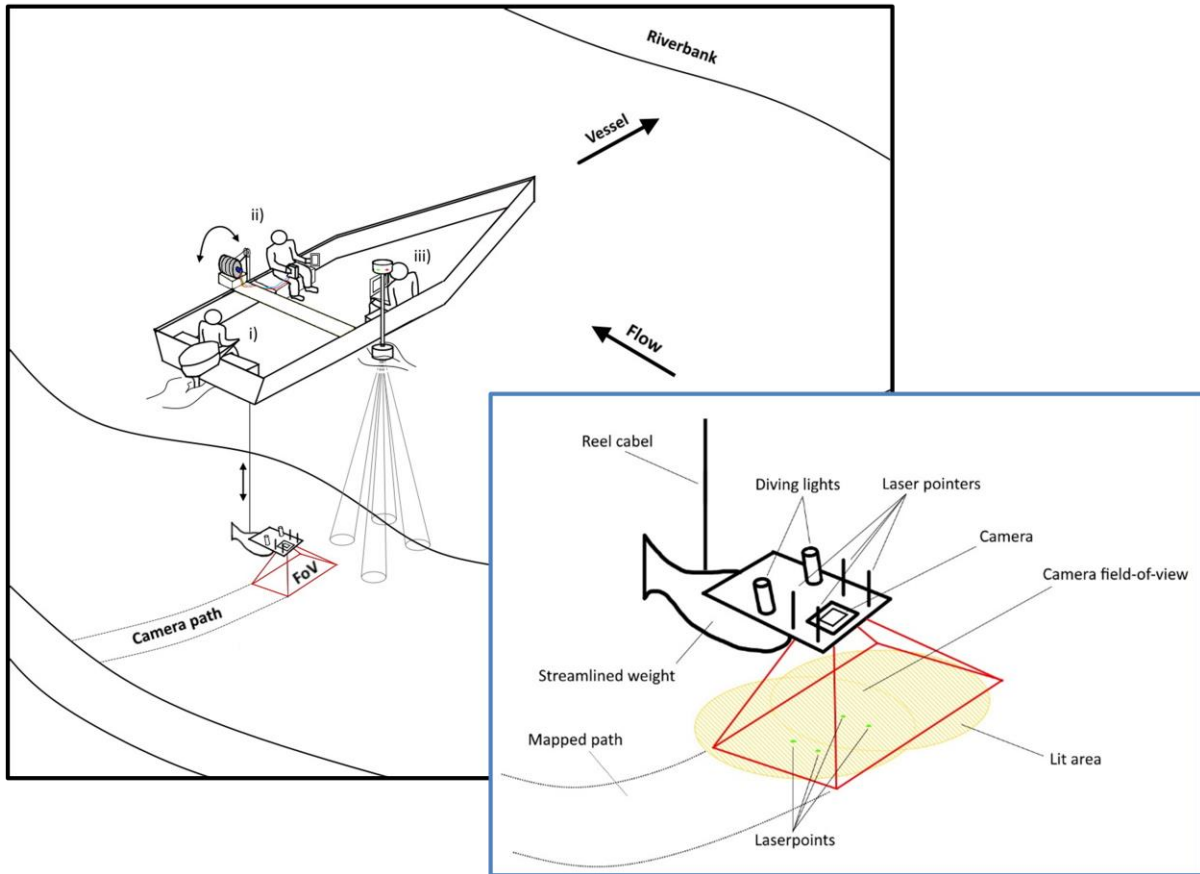
238

239

240

Fig. 3 presents a sketch of the measurement process with the equipment and a close-up of the underwater instrumentation. During the field measurements, the camera was attached to a streamlined weight (originally used as an isokinetic suspended sediment sampler) and lowered into the water from the vessel by an electric reel. The camera was positioned perpendicularly to the water and the riverbed, in front of the nose of the weight. Next to the camera, two diving lights worked as underwater light sources, focusing into the camera's field of view (FoV). In addition, four laser pointers were also equipped in hand-made isolation cases to provide possible scales for secondary measurements. They were also perpendicular to the bottom, projecting their points onto the underwater

241 camera field of view. Their purpose was to ensure a visible scale (mm/pixel ratio) in the video footages for
242 validation. During the measurement procedure, a vessel crossed the river slowly through river transects, while the
243 position of the above detailed equipment was constantly adjusted by the reel. Simultaneously, ADCP and RTK
244 GPS measurement were carried out by the same vessel, providing water depth, riverbed geometry, flow velocity,
245 ship velocity and position data. Based on this information and by constantly checking the camera's live footage
246 on deck, the camera was lowered or lifted to keep the bed in camera sight and avoid colliding with it. The sufficient
247 camera – riverbed distance depended on the suspended sediment concentration near the bed and the used
248 illumination. The reel was equipped with a register, with its zero adjusted to the water surface. This register was
249 showing the length of cable already released under the water, effectively the rough distance between the water
250 surface and the camera (i.e., the end of the cable). ~~Of course, d~~Due to the drag force this distance was not vertical,
251 but this value ~~was~~ ~~could be~~ continuously compared to the water depth measured by the ADCP. Differencing these
252 two values, an approximation for the camera – riverbed distance was given all time. The sufficient difference
253 could be established by monitoring the camera footage while lowering the device towards the bed. This value was
254 then to be maintained with smaller corrections during the survey of the given cross-section, always supported by
255 observing the camera recording, and adjusting to environmental changes. The vessel's speed was also adjusted
256 based on the video and slowed down if the video was blurry or the camera got too far away from the bed (see later
257 in Section 3.3). The measurements required three personnel to i) drive the vessel, ii) handle the reel, adjust the
258 equipment position, and monitor the camera footage, iii) monitor the ADCP data, while communicating with the
259 other personnel (see Fig. 3).



260
261
262
263

Figure 3: Left: sketch of the measurement process. The vessel was moving perpendicular to the riverbank along a cross-section (i). A reel was used to lower a camera close to the riverbed (ii). Simultaneously, the bed topography and water depth were measured by an ADCP (iii). Right: Close-up sketch of the underwater instrumentation.

264
265
266
267
268
269
270
271
272
273
274
275
276

The video recordings were made with a GOPRO Hero 7 and a Hero 4 commercial action cameras. Image resolutions were set to 2704x2028 (2.7K) with 60 frame per second (fps) and 1920x1080 (1080p) with 48 fps, respectively. Other parameters were left at their default (see GOPRO 2014; 2018), resulting in slightly different quality of produced images between the two cameras. We found that a 0.2-0.45 m/s vessel speed with 60 fps recording frequency was ideal to retrieve satisfactory images in a range of 0.4-1.6 m camera-bed distances. This meant approximately 15 minutes long measurements per transects. Further attention needed to be paid to the reel and its cable during the crossing when the equipment was on the upstream side of the boat. If the flow velocities are relatively high (compared to the total submerged weight of the underwater equipment), the cable can be pressed against the vessel-body due to the force from the flow itself, causing the reel cable to jump to the side and leave its guide. This results in the equipment falling to the riverbed and the measurement must be stopped to reinstall the cable. For illumination, a diving light with 1500 lumen brightness and 75° beam divergence, and one with 1800 lumen and 8° were used. The four lasers for scaling had 450-520 nm (purple and green) wavelength and 1-5 mW nominal power. Power supply was ensured with batteries for all instruments.

277
278
279
280
281
282

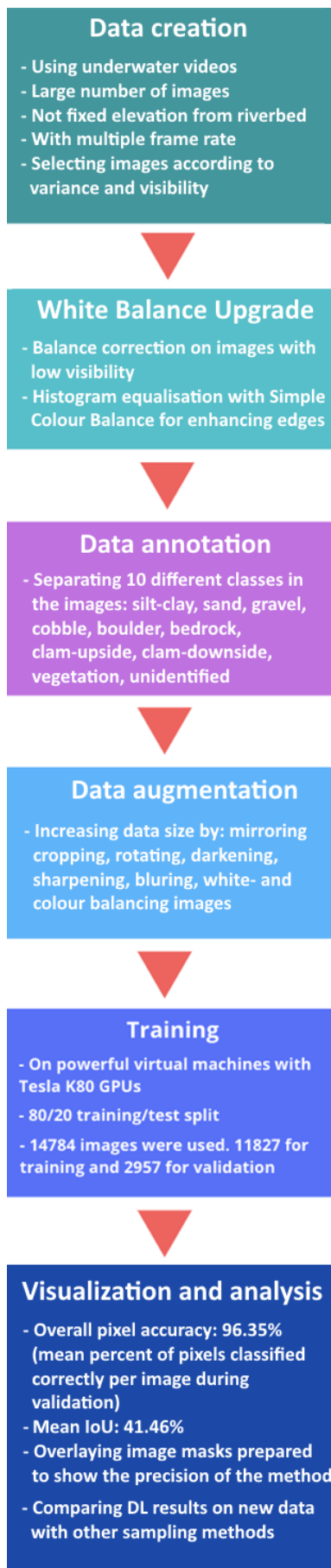
At Site A and Site B, conventional bed material (physical) samplings were also carried out by a grabbing (bucket) sampler along the analysed transects. At each cross-section 4-5 samples were taken, with one exception where we had 10. The measured GSDs were used to validate results of the AI algorithm. Separately, a visual evaluation of the videos was also carried out, where a person divided the transects into subsections based on their dominant sediment classes, after watching the footages.

283 2.3 Image analysis: Artificial Intelligence and the wavelet method

284 In this study, we built on the former experiences of the authors, using Benkó et al., 2020 as a proof-of-concept,
285 where the developed algorithm was applied for analysing drone videos of a dry riverbed. The same architecture
286 was used in this [study-manuscript](#), which is based on the widely used Google's DeeplabV3+ Mobilnet, in which
287 many novel and state-of-the-art solutions are implemented (e.g., Atrous Spatial Pyramid Pooling; Chen et al.,
288 2018). The model was implemented with Pytorch, exploiting its handy API and backward compatibility. The main
289 goal was to build a deep neural network model which can recognise and categorise (via semantic segmentation;
290 Chen et al., 2018) at least three main sediment size classes, i.e., sand, gravel and cobble, in the images, while
291 being quickly deployable. The benefit of the introduced method compared to conventional imagery methods lies
292 in the potential of automation and increased speed. If the annotation and training is carried out thoroughly,
293 analysing further videos can run effortlessly, while the computation time can be scaled down either vertically
294 (using stronger GPUs) or horizontally (increasing the number of GPUs; if parallel analysis of images is desired).
295 In this study a TESLA K80 24GB GDDR5 348bit GPU, an Intel Skylake Intel® Xeon® Gold 6144 Processor
296 (24.75M Cache, 3.50 GHz) CPU with 13GB RAM was used. Also, contrary to other novel image-processing
297 approaches in riverine sediment research (Buscombe, 2013; Detert and Weitbrecht, 2013), the deep convolutional
298 neural network is much less limited by image resolution and mm/pixel ratios, because it does not rely on precise
299 pixel count. This is an important advantage to be exploited here, as we perform non-scaled training and
300 measurements with the DL, i.e., camera-bed distance constantly changed, and size-reference was not used in the
301 images by the DL.

302

303 Fig. 4 presents the flowchart of our DL-based image processing methodology. The first step after capturing the
304 videos was to cut them into frames, during which the videos were exploded into sequential images. Our
305 measurement setup proved to be slightly nose-heavy. Due to this, and the drag force combined, the camera tilted
306 forward during the measurements. As a result, the lower parts of the raw images were sometimes too dark, as the
307 camera was looking over the riverbed, and not at the lit part of the bed. In this [study-manuscript](#), this problem was
308 handled by simply cutting out the lower 25% of the images as this was the region usually containing the dark,
309 unlit areas. Brightening and sharpening filters were applied on the remaining part of the images to improve their
310 quality. Next, the ones with clearest outlines and best visibility were chosen. This selection process was necessary
311 because this way the delineation process (learning the prominent characteristics of each class) can be executed
312 accurately, without the presence of misleading or confusing images, e.g., blurry or dark pictures where the features
313 are hard to recognise. For training purposes, we chose three videos from different sections each being ~15 minutes
314 long with 60 fps and 48 fps, resulting in 129 600 frames. In fact, such a large dataset was not needed due to the
315 strong similarity of the consecutive frames. The number of images to be annotated and augmented were therefore



decreased to ~2000. We also performed a white balance correction on some of the images to improve visibility, making it even easier to later define the sediment class boundaries. We used an additional algorithm to generate more data, with the so-called Simplest Colour Balance method (Limare et al., 2011). It is a simple, but powerful histogram equalisation algorithm which helps to equalise the roughness in pixel distribution.

These steps were followed by the annotation, where we distinguished ten classes: silt-clay, sand, gravel, cobble, boulder (mainly riprap), bedrock, clam-upside, clam-downside, vegetation, unidentified (e.g., wreckages). Annotation was carried out by a trained personnel, not by the authors, and performed with the help of an open-source software called PixelAnnotationTool (Breheret, 2017), which enables the user to colour mask large parts of an image based on colour change derivatives (i.e., colour masking part of the images which belong to the same class, e.g., purple/red – sand, green – gravel, yellow – cobble, etc.). The masks and outlines were drawn manually, together with the so-called watershed annotation. That is, when a line was drawn, the algorithm checked for similar pixels in the vicinity and automatically annotated them with the same class. The annotation was followed by a data augmentation step where beside mirroring, cropping, rotating the images (to decrease the chance of overfitting), we also convolved them with different filters. These filters added normally distributed noise to the photos to influence the watershed algorithm and applied sharpening, blurring, darkening, and white balance enhancement. Thus, at the data level, we tried to ensure that any changes in water purity, light, and transparency, as well as colour changes, were adequately represented during training. Images were uniformly converted to 960x540 resolution, scaling them down to make them more usable to fit in the GPU's memory. The next step was to convert all the images from RGB (Red-Green-Blue) based colour to grayscale. This is important because colour images have 3-channels, so that they contain a red, a green, and a blue layer, while grayscale images' pixel can only take one value between 0 and 255. With this colour conversion we obtained a threefold increase in computational speed. In total, a dataset of 14,784 human-annotated images was prepared (from the ~2000 images of the 3 training videos). The next step was to separate this dataset into training and validation sets. In this study, we used 80% of it ~~was used~~ for training the DL-Deep Learning algorithm, while 20% was withheld and reserved for the validation of the training. It was important to mix the images so that the algorithm selects batches in a pseudorandom manner during training, thus preventing the model from being

Figure 4: Flowchart of the applied methodology.

356 overfitted. Finally, after several changes in the hyperparameters (i.e., tuning), the evaluation and visualisation of
357 the training results were performed. Tuning is a general task to do when building DL-Deep Learning Networks,
358 as these hyperparameters determine the structure of the network and the training process itself. Learning rate, for
359 example, describes how fast the network refreshes, updates itself during the training. If this parameter is set too
360 high, the training process finishes quickly, but convergence may not be reached. If it is too low, the process is
361 going to be slow, but it converges. For this reason, nowadays the learning rate decay technique is used, where one
362 starts out with a large learning rate, then slowly reduces it. The technique generally improves optimization and
363 generalization of the DL-Deep Learning Networks (You et al., 2019). In our case, learning rate was initialised to
364 0.01, with 30000 iteration steps, and the learning rate was reset after every 5000 iterations with a decay of 0.1.
365 Another important parameter was the batch size, which sets the number of samples fed to the network before it
366 updates itself. Theoretical and empirical evidence suggest that learning rate and batch size are highly important
367 for the generalization ability of a network (He et al., 2019). In our study, a batch size of 16 was used (other general
368 values in the literature are 32, 64, 128, 256). We used a cross-entropy loss function.

369
370 ~~As previously mentioned, the training of the DL algorithm was managed without scaling, without the need for~~
371 ~~equipped lasers. However, we intended to use the laser pointers to provide a spatial scale for the recorded videos,~~
372 ~~as a secondary validation. As the lasers were not functioning as we originally hoped, we could not use them~~
373 ~~constantly during the cross-sectional surveys and could not aim for transactional scaling and validation this way.~~
374 ~~Instead, we diverted to validation in the points of the physical samplings as we could use the lasers in a few,~~
375 ~~selected points only. We used a textural image processing method to analyse the video images of these sampling~~
376 ~~spots. For this, the already mentioned, transferable wavelet based signal and image processing method was~~
377 ~~chosen. The method enables to calculate the image based grain size distribution of the selected pictures. The grey-~~
378 ~~scale intensity is analysed through pixel rows and columns of the image and handled as individual signals. Then,~~
379 ~~instead of Fourier transform, the less constrained wavelet transform is applied to decompose them. Finally,~~
380 ~~calculating the power spectra and the sizes (from pixel to millimetre, using the scale) of the wavelet components~~
381 ~~(each wavelet describes an individual grain) produces the grain size distribution for the given image. Beforehand,~~
382 ~~this method was proved to be the most efficient, non-DL image processing method for mixed sediments~~
383 ~~(Buscombe, 2013; 2020) and was already tested for underwater circumstances in an earlier study (Ermilov et al.,~~
384 ~~2020).~~

385 As previously discussed, the training of the deep learning (DL) algorithm proceeded without the application of
386 scaling, obviating the need for the laser equipment. Nevertheless, our original intention was to employ laser
387 pointers to establish a spatial scale for the recorded videos, serving as a supplementary validation measure.
388 Regrettably, the lasers did not operate as initially anticipated, rendering their continuous utilization during the
389 cross-sectional surveys and the pursuit of transactional scaling and validation unfeasible. Consequently, we shifted
390 our focus to validation at specific physical sampling points, where we could utilize the lasers properly. We adopted
391 a textural image-processing approach to analyse the video images captured at these sampling locations. In this
392 regard, we opted for the previously mentioned, transferable wavelet-based signal- and image-processing
393 technique. This method allows for the computation of the image-based grain size distribution from the selected
394 images. The analysis entails examining the grey-scale intensity along the pixel-rows and -columns within the
395 image, treating them as individual signals. This technique utilises the less-constrained wavelet transform, instead

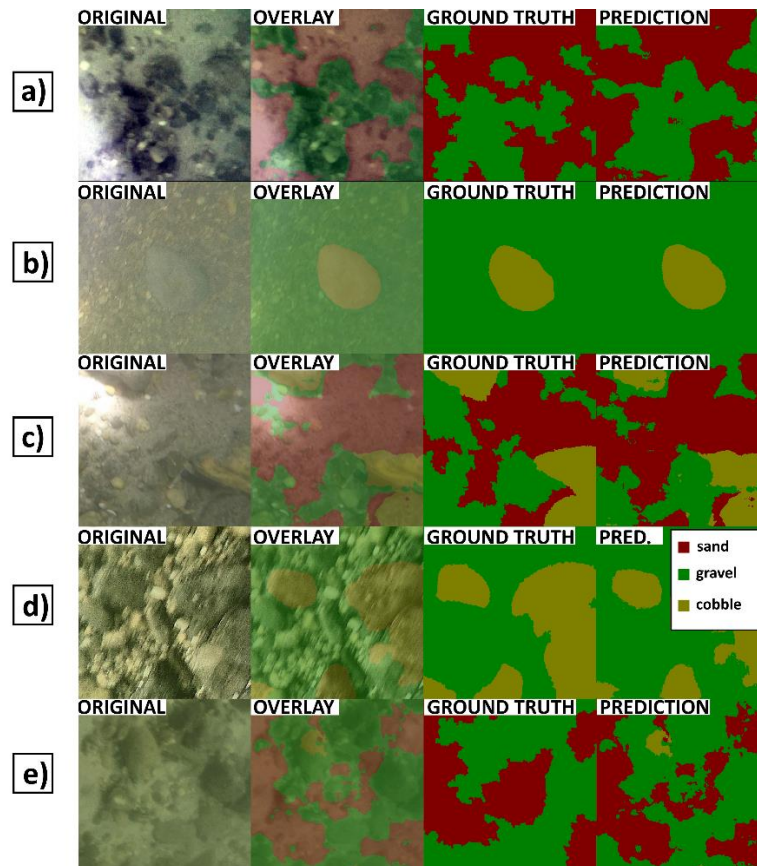
396 of the Fourier transform, to decompose these signals. Ultimately, by computing the power spectra and determining
397 the sizes (firstly in pixel, then changing to millimeter, using the scale) of the wavelet components (each
398 corresponding to an individual grain), the user can derive the grain size distribution for the given image. Prior to
399 this study, this methodology had demonstrated its efficiency as a non-DL image-processing technique for mixed
400 sediments (Buscombe, 2013; 2020) and had previously been tested by us, under underwater conditions as well
401 (Ermilov et al., 2020).

402 **3 Results and discussion**

403 **3.1 Evaluation of the training**

404 To evaluate the training process, the 2957 images of the validation set were analysed by the developed ~~DL-Deep~~
405 ~~Learning~~ algorithm and ~~its the given DL~~ results were then compared to their human-annotated counterparts. Fig.
406 5a-d shows results of original images (from the validation set), their ground truth (annotation by the training
407 personnel), as well as the DL prediction (result of the model). The overlays of the original and the predicted
408 images are also shown for better visualization. Calculating the overall pixel accuracy (i.e., the percent of pixels
409 that were correctly classified during validation) returned a satisfactory result with an average 96% match (over
410 the 2957 validation images, each having 960x540 resolution, adding up to a total of 1 532 908 800 pixels as
411 100%). As this parameter in object detection and ~~DL-Deep Learning~~ is not a stand-alone parameter (i.e., it can
412 still be high even if the model performs poorly), the mean IoU (intersection-over-union or Jaccard index) was also
413 assessed, indicating the overlap of ground truth area and prediction area, divided by their union (Rahman and
414 Wang, 2016). This parameter showed a much slighter agreement of 41.46%. Interestingly, there were cases, where
415 the trained model gave better result than the annotating personnel. While this highlighted the importance of
416 thorough and precise annotation work, it also showcased that the number of poor annotations was relatively low,
417 so that the algorithm could still carry out correct learning process and later detections, while not being severely
418 affected by the mistake of the training personnel. Fig. 5e showcases an example for this: the correct appearance
419 of cobble (yellow) in the prediction, even though the user (ground truth) did not define it during annotation. As a
420 matter of fact, these false errors also decrease the IoU evaluation parameter, even though they increase the
421 performance of the DL algorithm on the long term. Hence, this shows that pure mathematical evaluation may not
422 describe the model performance entirely. Considering that others also reported similar experience with ~~DL-Deep~~
423 ~~Learning~~ (Lu et al., 2018) and the fact that 40% and 50% are generally accepted IoU threshold values (Yang et
424 al., 2018; Cheng et al., 2018; Padilla et al., 2020), we considered the 41.46% acceptable, while noting that the
425 annotation and thus the model can further be improved. The general quality of our underwater images may have
426 also played a role in lowering the IoU result.

427

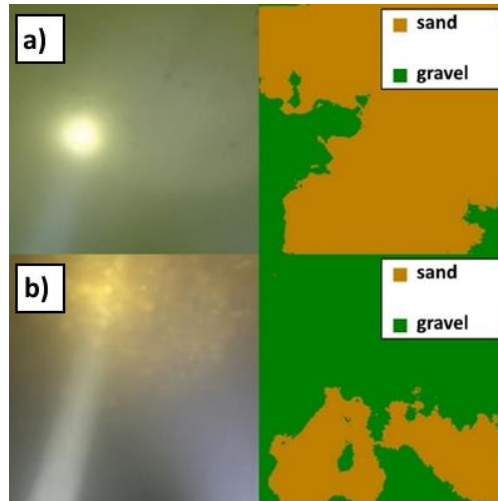


428
429
430
431
432
433
434

Figure 5: a-d) Example comparisons of ground truth (drawn by the annotating personnel, 3rd column) and DL predicted (result of analysing the raw image by the previously trained DL model, 4th column) during the validation process. The 1st column shows raw images, while the 2nd column overlays the result of the DL detection on the raw image for better visual context. e) Example of training personnel mistake during the annotation (i.e., lack of cobble/yellow annotation in ground truth) and how the DL performed better by hinting at the presence of the cobble fraction, leading to a false negative result during validation.

435
436
437
438
439
440
441
442
443

One of these quality issues for the DL algorithm was associated with the illumination. Using a diving light with small beam divergence proved counterproductive. The high intensity, focused light occasionally caused overexposed zones (white pixels) in the raw bed image, misleading the DL algorithm and resulting in detection of incorrect classes there (Fig. 6a). In darker zones, where the suspended sediment concentration was higher and at the same time, the effect of camera tilting was not completely removed by preprocessing, the focused light sometimes reflected from the suspended sediment itself and resulted in brighter patches in the images (Fig. 6b). This also caused false positive detections.



444
445 **Figure 6: The effect of strong diving light on the DL algorithm. a) Purely sand covered zone. b) Darker zone with**
446 **higher SSC. The original images are on the left, while the DL detections can be found on the right.**

447

448 3.2 Comparison of methods

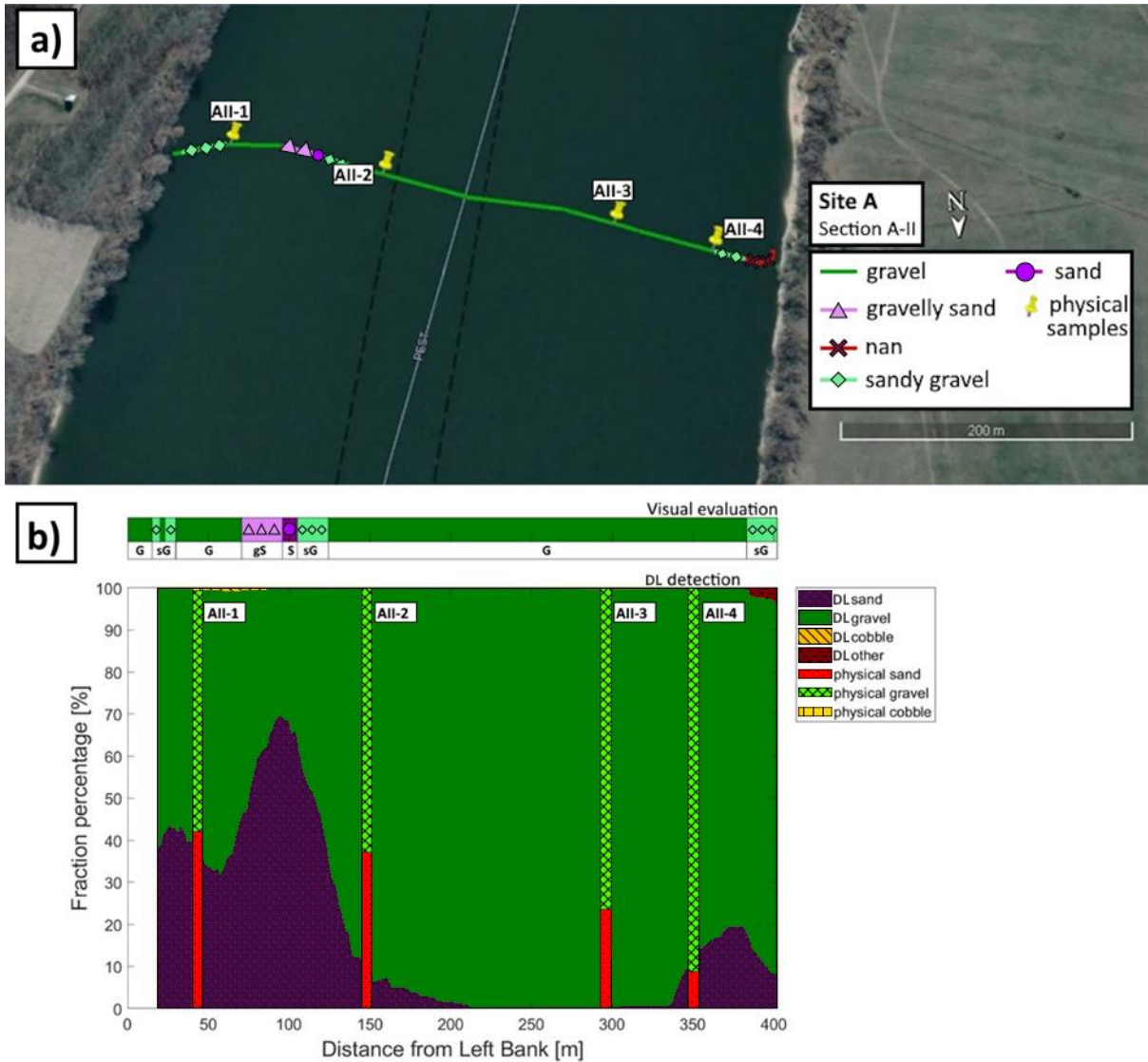
449 In each masked image, the occurring percentage of the given class (i.e., the percentage of the pixels belonging to
450 that class/colour mask, compared to the total number of pixels in the image) was calculated and used as the fraction
451 percentage in that given sampling point. These sediment classes reconstructed by the DL algorithm were then
452 compared to three alternative results: i) visual estimation, ii) GSD resulted from conventional grab sampling, iii)
453 wavelet-based image-processing. In the followings, results from two cross-sections will be highlighted, one from
454 Site A, the video used for the training, and one from Site B, being new for the DL. An averaging window of 15 m
455 was applied on each cross-sectional DL result to smoothen and despiked the dataset. The interval of physical sample
456 collection in wider rivers can range anywhere between 20-200 m within a cross-section, depending on the river
457 width and the homogeneity of riverbed composition. The averaging window size was chosen to be somewhat
458 lower than our average applied physical sampling intervals in this study, but still in the same order of magnitude.
459 The scope of the present ~~study-manuscript~~ did not include further sensitivity analysis of the window size. In the
460 followings, the reader is led through the comparison process via the example of two transects, and is given the
461 over-all evaluation of the accuracy of the method.

462 3.2.1 Visual evaluation and physical samples

463 ~~In Fig. 7a, the path of the vessel can be seen in Section A—II, at Site A. The path was coloured based on the visual~~
464 ~~evaluation of the riverbed images. The different colours represent the dominant sediment type seen at the given~~
465 ~~point of the bed. The locations of the physical bed material samplings are also shown (see yellow markers). App.~~
466 ~~Fig. A1 presents the raw (i.e., before moving-average) results of the DL-detection of each analysed image along~~
467 ~~Section A—II. Currently, our approach is sensitive and large spikes, differences can occur in the DL-detection~~
468 ~~between consecutive, slightly displaced video frames. Due to this, and the fact that there is uncertainty in the~~
469 ~~coordinates of the underwater photos and their corresponding physical samples, it is not recommended to carry~~
470 ~~out comparisons by selecting certain image and its DL-detection. Instead, we applied a moving-average based~~
471 ~~smoothing for each raw, cross-sectional DL-detection, with a window size corresponding to 15 m at each site.~~
472 ~~These moving-averages are later used to compare in the sampling points to the physical sampling and the wavelet~~

473 method. For illustration purposes, we provided the raw DL detections of all the sampling point images in the
474 Appendix, even though their result may not be representative of their corresponding moving average values. Fig.
475 7b shows the cross-sectional visual classification compared to the DL detected sediment fractions in percentage
476 after applying moving average (i.e., the smoothed version of App. Fig. A1). The noises are mostly caused by
477 sudden changes in lighting conditions. It happens either from losing visual on the riverbed momentarily due to
478 sudden topography changes or from increased suspended sediment concentration. The DL result shows
479 satisfactory match with the human evaluation. For example, around 100 m from the left bank, between AII-1 and
480 AII-2 sampling points, the DL algorithm peaks with around 70% sand and 30% gravel correctly. Furthermore, on
481 the two side of this peak a steep transition to gravel and decreasing sand occurs, similarly to the visual observation,
482 marked as sandy gravel and gravelly sand. Mixed sediment zones were also correctly identified by the DL
483 algorithm at both riverbanks. In Fig. 7a, we depict the vessel's trajectory within Section A – II at Site A. The path
484 is color-coded based on our visual assessment of the riverbed images, with distinct colors representing the
485 prevalent sediment type at each specific location on the riverbed. Additionally, we have marked the positions of
486 physical bed material samples with yellow markers for reference. App. Fig. A1 presents the unprocessed results
487 of the DL detection for each analysed image along Section A – II, prior to any moving-average smoothing. It's
488 important to note that our current approach is highly sensitive, occasionally resulting in substantial fluctuations in
489 DL detection between successive, slightly displaced video frames. Owing to this sensitivity and the inherent
490 uncertainty in the coordinates of the underwater photos and their corresponding physical samples, we discourage
491 making direct comparisons by selecting a specific image and its DL detection. Instead, we have implemented a
492 moving-average-based smoothing technique for each raw, cross-sectional DL detection, using a window size of
493 15 meters at each site. These moving averages serve as the basis for comparisons with the physical sampling data
494 and the wavelet method. For the sake of clarity, we have included the raw DL detections of all sampling point
495 images in the Appendix, although these results may not precisely reflect their corresponding moving-average
496 values. In Fig. 7b, we present a comparison between the cross-sectional visual classification and the DL-detected
497 sediment fractions in percentage after applying the moving-average smoothing (i.e., the smoothed version of App.
498 Fig. A1). Any noise observed in these results is primarily attributable to abrupt changes in lighting conditions,
499 which can occur either when visual contact with the riverbed is momentarily lost due to sudden bathymetrical
500 changes or as a result of increased suspended sediment concentration. Overall, our DL results exhibit a
501 commendable concordance with human evaluations. For instance, in the vicinity of 100 meters from the left bank,
502 between sampling points AII-1 and AII-2, the DL algorithm correctly identifies a peak with approximately 70%
503 sand and 30% gravel. Moreover, on either side of this peak, a steep transition to gravel and a decline in sand
504 content are observed, consistent with visual observations, which we have labelled as "sandy gravel" and "gravelly
505 sand." The DL algorithm also accurately identifies mixed sediment zones on both riverbanks.

506



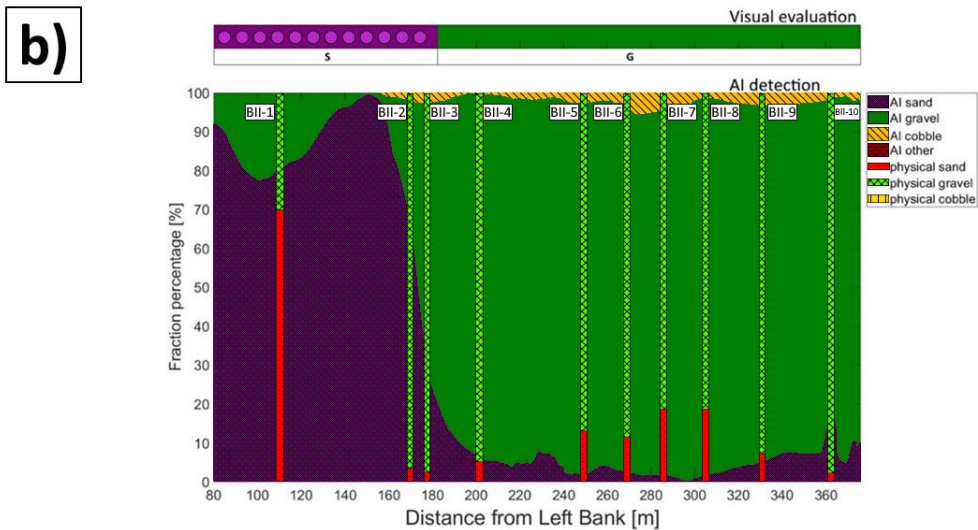
507

508 **Figure 7: a)** The path of the vessel and camera in Section A – II, Site A. The polyline is coloured based on the sediment
 509 features seen during visual evaluation of the video. Yellow markers are the locations of physical bed material samplings.
 510 (Map created with Google Earth Pro). **b)** The visual evaluation of the dominant sediment features in the video (top)
 511 compared to sediment fraction percentage, recognised by the DL algorithm (bottom). DL result after applying moving-
 512 averaging. The visual evaluation included four classes: gravel – G, sandy gravel – sG, gravelly sand – gS, sand – S).
 513 The fractions of the physical samples are shown as verticals.

514

515 At site B (Fig. 8a) the river morphology is more complex compared to Site A as a groyne field is located along
 516 the left bank (see Fig. 2b). As such, the low flow regions between the groynes yield the deposition of fine
 517 sediments, and much coarser bed composition in the narrowed main stream. As it can be seen, the DL algorithm
 518 managed to successfully distinguish these zones: the extension of fine sediments in the deposition zone at the left
 519 bank were adequately estimated and showed a good match with the visual evaluation for the whole cross-section
 520 (see Fig. 8b).

521



522
 523 **Figure 8: a) The path of the vessel and camera in Section-B – II, Site B. The polyline is coloured based on the sediment**
 524 **seen during visual evaluation of the video. Yellow markers are the locations of physical bed material samplings. (Map**
 525 **created with Google Earth Pro). b) Sediment fraction percentages in Section-B – II, recognised by the AI. The visual**
 526 **evaluation included two classes: gravel – G, sand – S). The fractions of the physical samples are shown as verticals.**

527
 528 Results of the other measurements can be found in the Appendix. App. Fig. C2, D2 and E2 show that the trend of
 529 riverbed composition from the visual evaluation is well-captured by the DL algorithm in the other cross-sections
 530 of the study as well.

531
 532 Next, the physically measured and DL-detected relative proportion of sand, gravel and cobble fractions were
 533 compared in each of the 27 sampling points. Firstly, however, outliers or incomparable data had to be identified.
 534 In our case, this meant the separation of sampling points where the differences between the results of the two
 535 methods were independent from the efficiency and performance of the DL algorithm. This selection was carried
 536 out after analysing the grainsize distribution curves of the weight-sieved physical samples (App. Fig. F1) and the
 537 riverbed images around the sampling points (App. Fig. A3, B1, C4, D4, E4). Based on our findings, the outliers

538 have been identified and separated into Outlier Type A, and Outlier Type B categories. First category included
539 the sampling points where the GSD curves showcased bimodal (gap graded) distributions. This type of riverbed
540 sediment distribution is a typical sign of riverbed armouring (Rákóczi, 1987; Marion & Fraccarollo, 1997), where
541 a coarse surface layer protects the underlying finer subsurface substrate (see e.g., Wilcock, 2005). While the
542 camera only sees the upper layer, the bucket sampler can penetrate the surface and gather sample from the
543 subsurface as well. As a result, the two methods cannot be compared solely on the surface distribution. In App.
544 Fig. A2, supportive images of bed armouring are provided, taken during our surveys in the Upper section of the
545 Hungarian Danube. Out of the 27 sampling points, 11 were affected by armouring and categorised as Outlier
546 Type A. The category of Outlier Type B consisted of points from the opposite case: where the riverbed image
547 contained fine sediment, but the physical samples did not. In these cases, a relatively thin layer of fine sediment
548 covered the underlying gravel particles. 2 sampling points were categorised as Outlier Type B, both of which were
549 near to the borderline between a deposition zone behind a groyne, and the gravel bedded main channel. In these
550 cases, the bucket sampler probably either stirred up the deposited fine sediment and washed it down during its
551 lifting or was dragged through purely gravel bedded patch during sampling, as the surface composition was rapidly
552 changing on this before-mentioned borderline. It is important to highlight that the analysis of physical samples
553 involves measuring and weighing various sediment size classes, leading to weight distribution. In contrast,
554 imaging methods offer surface distributions, and as a consequence, the presence of a thin layer of fine sediments
555 on the surface can significantly skew the resulting composition (Bunte and Abt, 2001; Sime and Ferguson, 2003;
556 Rubin et al., 2007). ~~It is also worth noting that the physical samples are analysed by weighing the different~~
557 ~~sediment size classes, resulting in weight distribution. On the other hand, the imagery methods provide surface~~
558 ~~distributions, hence having a thin layer of fine sediments on the top can strongly bias the resulted composition~~
559 ~~(Bunte and Abt, 2001; Sime and Ferguson, 2003; Rubin et al., 2007).~~

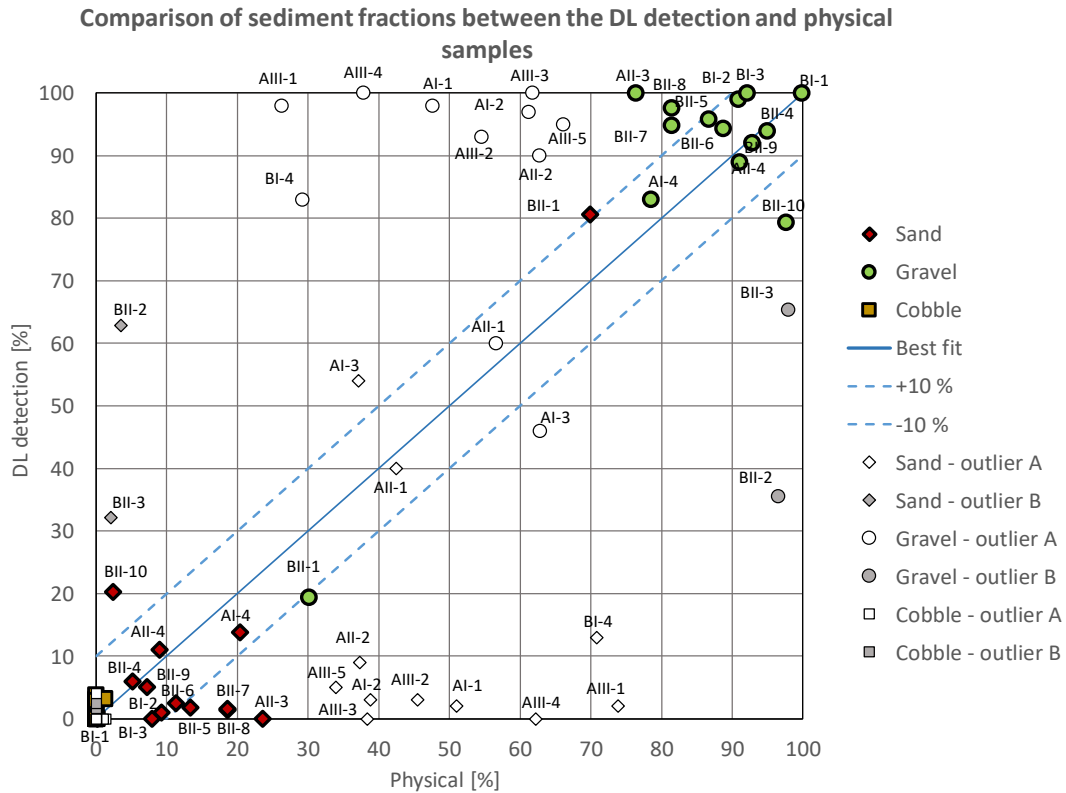
560

	Comparable data	Outlier Type A	Outlier Type B	Σ
No. sampling points	14	11	2	27

561 **Table 2: After evaluating the results of the sieving analyses and riverbed surface images, out of the 27 sampling points,**
562 **14 were defined as comparable between the applied sampling methods. 11 points were categorised as Outlier Type A,**
563 **because their GSD curves were bimodal. 2 points were defined as Outlier Type B, since their images showed the**
564 **presence of fine sediment, while the sieve analyses did not.**

565

566 Overall, the DL-based classification agreed well within the comparable sampling points, with an average error of
567 4.5% (Fig. 9). It can be seen that even though in outlier points AII-1 and AI-3 the DL algorithm coincidentally
568 gave good match with the sieving analysis, in the rest of the outlier points the DL- and physical-based results
569 systematically differ from each other, supporting our outlier selection methodology.



570
571
572
573
574
575

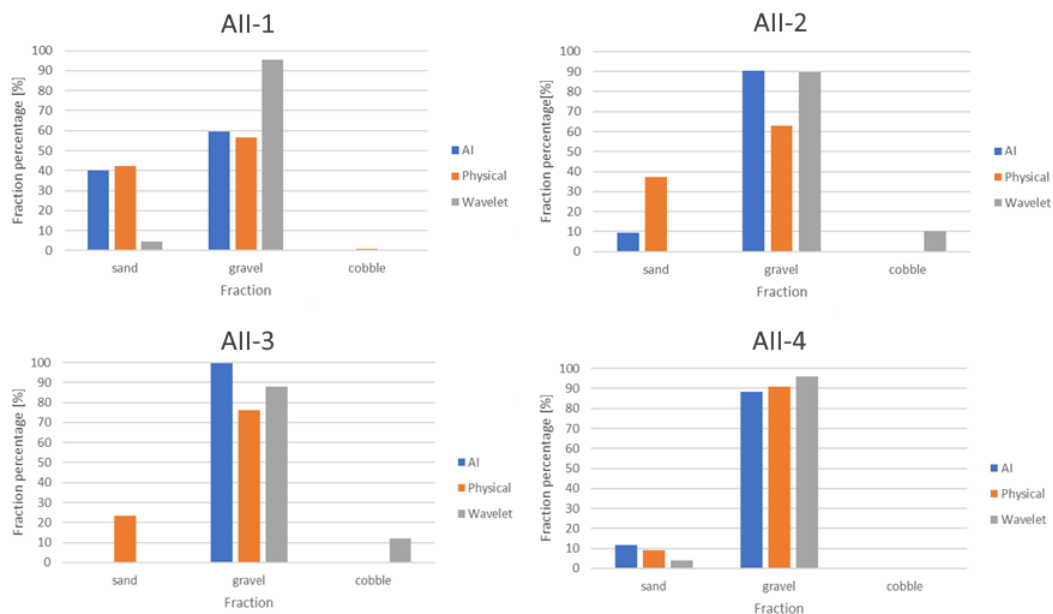
Figure 9: Comparison of relative sediment fractions between the DL detection and physical samples. The three main sediment types (sand-gravel-cobble) are marked with different colour and symbols. The name of the sampling points where the given relative proportion was measured/detected is also written for gravel and sand (cobble was negligible). The proportions of outlier sampling points are marked with white/grey, while the symbol represents the sediment type respectively. The comparable points have their proportions with green (gravel) and red (sand) symbols.

576

577 3.2.21 Wavelet analysis

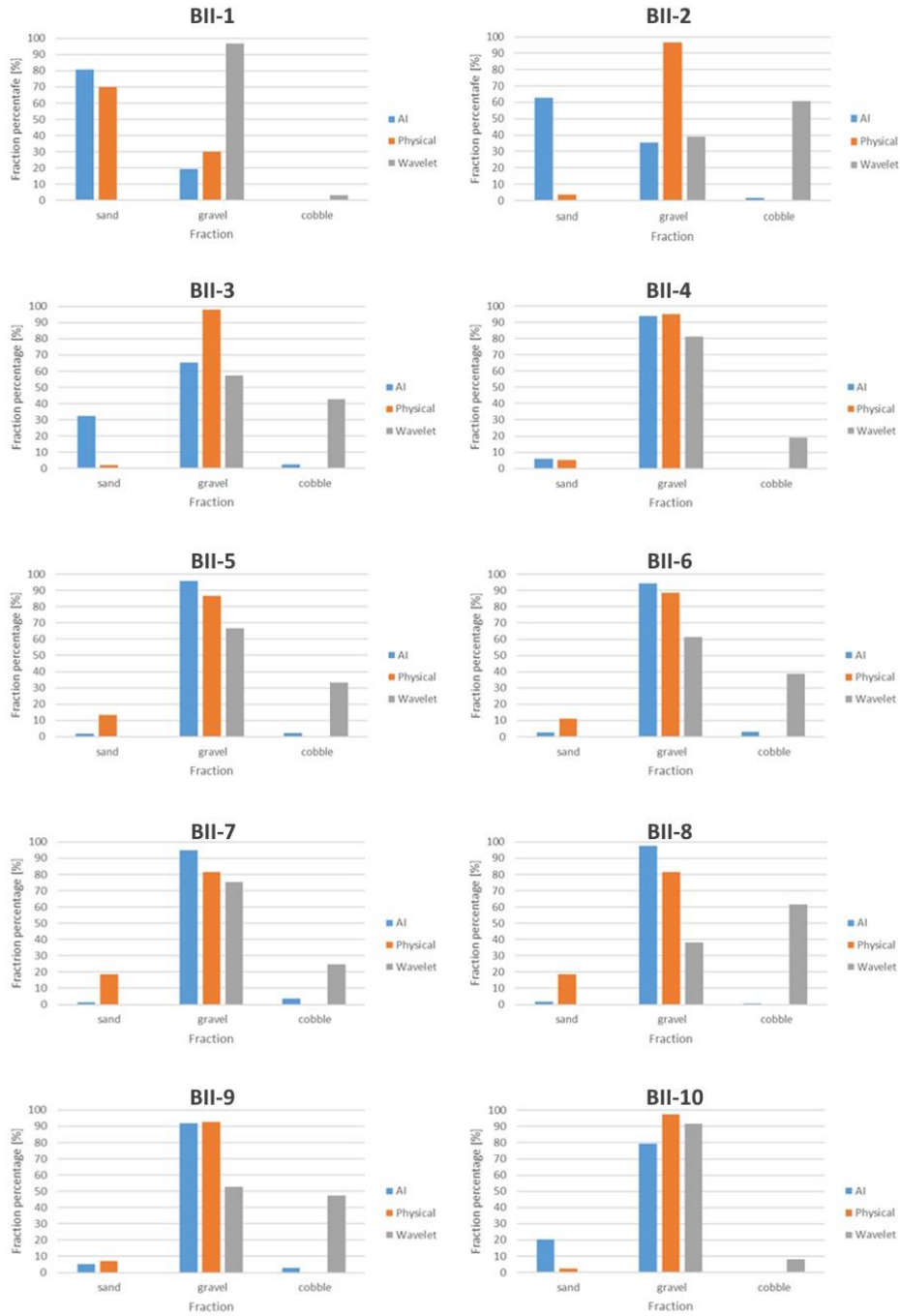
578 Regarding the wavelet analysis-based imaging technique, it is evident that there is a slight overall overestimation
 579 of coarse particles, and the accurate reconstruction of sand classes is not achieved. This observation aligns with
 580 our earlier field experiences reported in Ermilov et al. (2020), where we highlighted the wavelet technique's
 581 pronounced sensitivity to image resolution. We demonstrated that to successfully detect a grain, its diameter must
 582 be at least three times larger than a pixel. In the subsequent analysis, we compare the sediment proportions
 583 determined by the wavelet-based method to those obtained earlier through DL and physical-based approaches,
 584 presenting the results in bar plots (Fig. 10, 11). For instance, when the camera was positioned closer to the riverbed
 585 at sampling points AII-1 and AII-4, resulting in a more favourable mm/pixel ratio, the wavelet algorithm was able
 586 to detect coarse sand accurately. However, it struggled to identify finer sand, leading to lower sand percentage
 587 estimates (Fig. 10). In other sampling points where sand particles were below the resolution limit, the wavelet
 588 method consistently identified the presence of cobbles instead (Fig. 10), a distinction not made by the other two
 589 methods. This pattern broadly characterizes the wavelet method's performance during our study. For illustrative
 590 purposes, we provide an example highlighting the differences in the capabilities of these two methods in Figure
 591 12. While both methods detect the presence of two major sediment categories, the wavelet technique interprets

592 the information as a mixture of gravel and cobbles, whereas the DL algorithm recognizes the presence of sand
 593 coverage and gravel particles.
 594 As for the wavelet analysis based imagery technique, an overall slight overestimation of the coarse particles can
 595 be observed, and the sand classes are, in fact, not reconstructed correctly. This finding agrees well with the field
 596 experiences of Ermilov et al. (2020), where the authors indicated the strong sensitivity of the wavelet technique
 597 on the image resolution, and showed that to detect a grain, the diameter must be at least three times larger than
 598 the pixel. In the following, the wavelet detected relative sediment proportions are compared to the earlier,
 599 corresponding DL, and physical based ones via bar plots (Fig. 10, 11). For example, the camera was closer to the
 600 riverbed at sampling points AII-1 and AII-4, resulting in a better mm/pixel ratio, hence the wavelet algorithm was
 601 able to detect coarse sand, but finer sand was neglected yielding the lower sand percentages (Fig. 10). In the other
 602 sampling points, where sand was below its resolution, the wavelet method systematically measured the presence
 603 of cobbles instead (Fig. 10), even though the other two methods did not. This trend generally described the
 604 performance of the wavelet method during our study. For visual purposes, an example of the difference in the
 605 capabilities of the two method is given in Fig. 12. While both detected the presence of two major sediment
 606 categories, the wavelet translated the information as gravel and cobble mixture, meanwhile the DL algorithm
 607 recognised the sand coverage and gravel particles.
 608



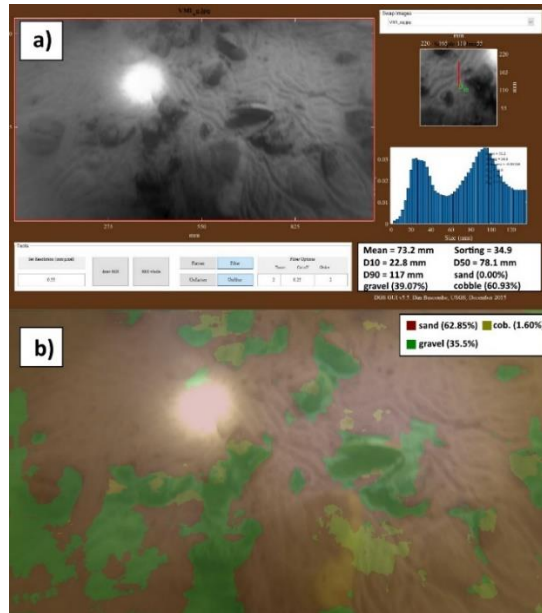
609 **Figure 10: Comparison of relative sediment fraction proportions [%] at the sampling locations from the moving-**
 610 **averaged DL detection, conventional sieving and the wavelet-based image processing method. Section A – II.**
 611

612



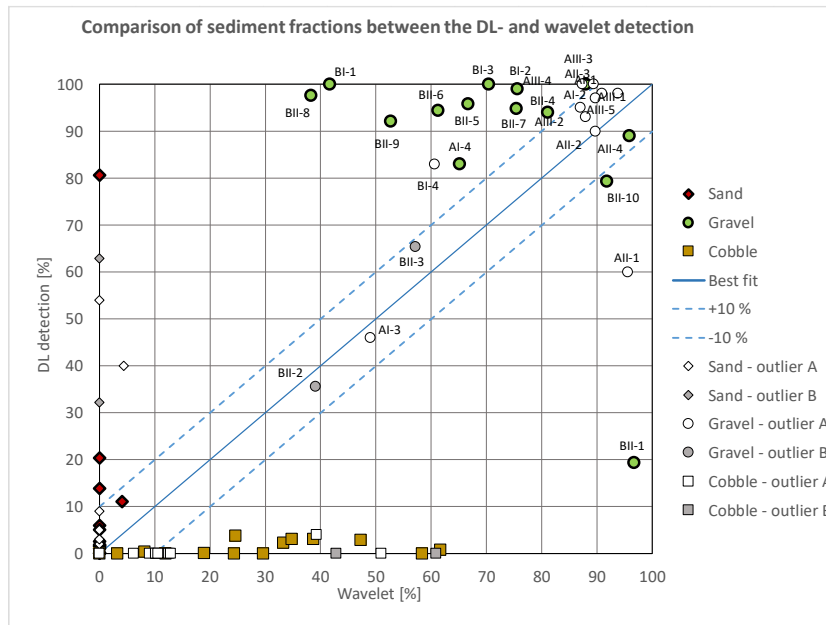
613
614
615

Figure 11: Comparison of relative sediment fraction proportions [%] at the sampling locations from the moving-averaged DL detection, conventional sieving and the wavelet-based image processing method. Section-B = II.



616
 617 **Figure 12: a) Wavelet analysis result of the underwater image in BII-2. b) DL detection result of the same image.**

618
 619 Overall, the comparison between the two image-based method showed greater discrepancies (Fig. 13), due to the
 620 limitations of the wavelet approach, discussed earlier. The same sampling points were labelled as outliers as
 621 earlier. As it can be seen, the wavelet significantly differed in the points where the physical samples and DL-
 622 detections matched (green data points), due to its excessive, false cobble detections. However, it showed good
 623 agreement with the DL in most of the outlier points, supporting the earlier observation: the surface in those points
 624 was composed of solely gravel, and the finer fractions of the physical samples must have come from the
 625 subsurface. Hence, the outlier selection process was well based.



626
 627 **Figure 13: Comparison of sediment fractions between the DL detection and the wavelet approach, for the selected**
 628 **sampling points. The three main sediment types (sand-gravel-cobble) are marked with different colour (red-green-**
 629 **yellow) and symbols (diamond-circle-square) respectively. The name of the sampling points where the given relative**
 630 **proportion was measured/detected is also written for gravel. The proportions of outlier sampling points are marked**
 631 **with white/grey, while the symbol represents the sediment type respectively. The comparable points have their**
 632 **proportions with green (gravel), red (sand) symbols.**

633
634 Based on the results presented in this study manuscript, it could be established that the DL algorithm managed to
635 recognise the main features of the riverbed material composition from underwater videos with satisfactory
636 accuracy in the comparable sampling points (based on the sieving analysis of physical samples) and along cross-
637 sections (based on the visual evaluation). The method showed good potential for mapping heterogenous riverbeds
638 along river cross-sections. Furthermore, the wavelet proved to be a limited comparison tool with the introduced
639 field measurement methodology, as this latter did not provide it with the sufficient resolution most of the time.

640

641 3.3 Implementation challenges

642 ~~The power supply for the entire imaging infrastructure, i.e., for the camera, the diving lights and lasers, was~~
643 ~~ensured by batteries. However, due to the low temperature at the river bottom, the battery level decreased~~
644 ~~extremely fast, compared to normal circumstances. Providing the power supply directly from the motorboat can~~
645 ~~overcome this issue. Keeping the camera in the adequate height also caused difficulties, since getting too close to~~
646 ~~the bed can harm the devices, lifting too high, on the other hand, will result in poor image quality. The measured~~
647 ~~instantaneous ADCP flow depth data was used therefore to keep the bed in camera sight, while maintaining proper~~
648 ~~boat velocity to avoid blurry images. Choosing a higher recording frequency and decreasing exposure time,~~
649 ~~however, can be beneficial and alter this limitation, when provided. Lower velocities could not be maintained as~~
650 ~~the river would have moved the vessel out of the section. An alternative solution can be to move on longitudinal~~
651 ~~(streamline) paths instead of transects. This would allow for lower vessel speed. This would increase the time of~~
652 ~~the measurement, which still could be profitable if the images are of higher quality. However, the conventional~~
653 ~~way for river bathymetry surveys is to move on transversal, cross sectional paths, due to the river bathymetry~~
654 ~~having a lower spatial variation along streamlines, compared to the changes that occur in the transversal direction~~
655 ~~(Benjankar et al., 2015; Kinsman, 2015). As such, it may require carrying out a relatively dense set of longitudinal~~
656 ~~paths to gain proper information, further increasing the time demand. Thus, for this alternative, higher attention~~
657 ~~needs to be paid towards choosing these paths and the interpolation method. Another challenge can be the~~
658 ~~influence of drag force on the measurement setup. In our case, even though the main body itself was a streamlined~~
659 ~~weight, equipping the other tools on it turned the setup geometry irregular. Additionally, we found that our setup~~
660 ~~was a bit nose heavy. On the long term however, this effect could be reduced by building a streamlined container~~
661 ~~(e.g., 3D printed body, or a body similar to unmanned underwater vehicles') with slots in it for each device, and~~
662 ~~also by improving the weight distribution. Furthermore, we hypothesize that by using lasers (as originally planned~~
663 ~~in this study) during the measurements, the known structure (i.e., the position and distances) of the laser points'~~
664 ~~projection when the setup is perpendicular to the bed, can help to orthorectify the images. This will decrease the~~
665 ~~effect of occasional tilting when one wishes to carry out size analysis on the images. In our case, we presented~~
666 ~~how the wavelet method had inherently bigger issues (i.e., image resolution limit) when used with the introduced~~
667 ~~methodology, which could not be caused by the tilting of the camera since those would be in a significantly lower~~
668 ~~magnitude of error.~~

669 The power supply for the entire imaging infrastructure, including the camera, diving lights, and lasers, relied on
670 batteries. However, due to the lower temperatures at the river bottom, the battery depletion rate was significantly
671 accelerated compared to typical conditions. To address this issue, we explored the option of a direct power supply
672 from the motorboat. Ensuring the camera's optimal positioning posed challenges as well. Proximity to the riverbed

673 risked damage to the equipment, while excessive camera-bed distances compromised image quality. To maintain
674 a clear view of the riverbed while avoiding blurry images, we utilized real-time ADCP water depth data to adjust
675 the camera's position, while simultaneously optimizing the boat's velocity. Increasing the recording frequency and
676 reducing exposure time emerged as potential solutions to mitigate this limitation. Lower vessel velocities were
677 not feasible, as they would have caused the vessel to drift out of the desired section. Alternatively, moving along
678 longitudinal (streamline) paths rather than transects may present the opportunity for slower vessel speeds,
679 potentially resulting in higher-quality images in the future. However, the conventional approach for river
680 bathymetry surveys typically involves transversal paths due to lower spatial variations along streamlines
681 compared to the transverse direction (Benjankar et al., 2015; Kinsman, 2015). Therefore, implementing
682 longitudinal paths may require a denser network to obtain sufficient data, thus increasing time demands. Hence,
683 careful consideration of path selection and interpolation methods becomes critical for this alternative approach.
684 Another challenge pertained to the impact of drag force on the measurement setup. Although the main body had
685 a streamlined design, the addition of other tools disrupted the setup's geometry. Additionally, we encountered a
686 slight imbalance in weight distribution. Long-term solutions could involve constructing a streamlined container
687 (e.g., a 3D-printed body or a body resembling unmanned underwater vehicles) with designated slots for each
688 device and improving weight distribution. Furthermore, we hypothesized that using lasers (as originally planned
689 in this study) during measurements could assist in orthorectifying the images, leveraging the known structure and
690 positioning of laser points' projections when the setup is perpendicular to the riverbed. This could reduce the
691 impact of occasional tilting, which may affect size analysis if scaling is included. In our specific case, we
692 demonstrated that the wavelet method had inherent limitations (e.g., image resolution limits) when applied within
693 our methodology, issues not attributable to camera tilting, as these would have had a significantly lower error
694 magnitude.

695
696 As for the training of the DL algorithm with the underwater images, the illumination is indeed a more crucial
697 aspect, compared to normal imagery methods. In many cases only the centre areas of the images were clearly
698 visible, whereas the remaining parts were rather dark and shady. Determining the boundaries between distinct
699 sediment classes for these images was challenging even for experienced eyes. This quality issue generated
700 incorrect annotations at first. To overcome this issue, manually varying the white balance thus enhancing the
701 visibility of the sediment could improve the results of the training. It is known that when DL-Deep Learning
702 methods are to be used, most of the problems arise from the data side (Yu et al., 2007), whereas issues related to
703 the applied algorithms and hardware are rare. This is because data is more important from an accuracy perspective
704 than the actual technical infrastructure (Chen et al., 2020). The time demand of image annotation (data
705 preparation) is relatively high, i.e., a trained person could analyse roughly 10 images per hour. On the other hand,
706 as introduced earlier, a great advantage of using DL is the capability of improving the quality of training itself,
707 often yielding better agreement with reality, compared to the manual annotation. Similar results have been
708 reported by Lu et al., (2018). This at the same time proves that with the introduced approach, there is no need for
709 very precise manual training, thus a fast and effective training process can eventually be achieved.

710
711 The validation of the DL-Deep Learning algorithm is far from straightforward. In this study, four approaches were
712 adopted: adapted, a mathematical approach, and comparison with three other measurement methods, respectively.

713 The mathematical approach was based on calculating pixel accuracy and the Intersection-over-union parameter,
714 as it is usually done in case of DL-Deep Learning methods to describe their efficiency (e.g., Rahman and Wang,
715 2016). However, the DL model in some cases overperformed, and provided more accurate results for the sediment
716 composition than the human annotator did. This meant the calculated difference between the annotated validation
717 images and their responding DL-generated result was not solely originated from underperformance of the DL-
718 model, but from human error as well. Consequently, using only the mathematical evaluation in this study could
719 not describe adequately the model performance. Hence, the results were compared to those of three other methods:
720 i) visual evaluation of the image series, ii) a wavelet-based image-processing method (using the method of
721 Buscombe, 2013) and iii) riverbed composition data from physical samples. Considering the features of the
722 applied methods, the first one, i.e., the visual observation, is expected to be the most suitable for the model
723 validation. Indeed, when assessing the bed surface composition by eye, the same patterns are sought, i.e., both
724 methods focus on the uppermost sediment layer. On the other hand, the physical sampling procedure inherently
725 represents subsurface sediment layers, leading to different grain size distributions in many cases. For instance, as
726 shown earlier, if bed armour develops in the riverbed and the sampler breaks-up this layer, the resulted sample
727 can contain the finer particles from the subsurface. On the contrary, in zones where a fine sediment layer is
728 deposited on coarse grains, i.e., a sand layer on the top of a gravel bed, the physical samples represent the coarse
729 material too, moreover, considering that the sieving provides weight distribution this sort of bias will even enhance
730 the proportion of the coarse particles. Attempts were made to involve a third, wavelet-based method for model
731 validation. However, this method failed when finer particles, i.e., sand, characterized the bed. This is an inherent
732 limitation of these type of methods, as discussed earlier, i.e., when the pixel size is simply not fine enough to
733 reconstruct the small grain diameters in the range below fine gravel. Lastly, the most comparable sample points
734 were selected to quantify the performance of the DL. Holding the sieved physical samples as ground truth, the DL
735 algorithm showed promising results. The average error (difference) between DL-detected and physically
736 measured relative sediment fraction portion percentages was 4.5%. Furthermore, the DL algorithm successfully
737 detected the trend of changing bed composition along complete river cross-sections.

738

739 As it is known, the ML and DL models can learn unknown relationships in datasets, but unwanted biases as well.
740 With our current dataset, these biases would be the darker tones of visible grain texture and the lack of larger grain
741 sizes. This way our model in its current state is only applicable effectively in the chosen study site, until the dataset
742 is not expanded with additional images from other rivers or regions. However, the purpose of the study-manuscript
743 was to introduce the methodology itself and its potential in general and not to create a universal algorithm.

744 **3.4 Novelty and future work**

745 The introduced image-based DL-Deep Learning algorithm offers novel features in the field of sedimentation
746 engineering. First, to the authors' knowledge, underwater images of the bed of a large river have not yet been
747 analysed by AI. Second, the herein introduced method enables extensive mapping of the riverbed composition, in
748 contrast to most of the earlier approaches, where only several points or shorter sections were assessed with
749 imagery methods. Third, the method is much faster compared to conventional samplings or non-DL-based image-
750 processing techniques. The field survey of a 400 m long transect took ~15 minutes, while the DL analysis took 4
751 minutes (~~approx~~approx. 7 image/s). The speed range of 0.2-0.45 m/s of the measurement vessel and the 15 minutes

752 per transect complies with the operating protocol of general ADCP surveys on rivers (e.g., RD Instruments, 1999;
753 Simpson, 2002; Mueller and Wagner, 2013). Hence, the developed image-based measurement can be carried out
754 together with the conventional boat-mounted ADCP measurements, further highlighting its time efficiency.
755 Hence, the method offers an alternative approach for assessing riverbed material on-the-go, in underwater
756 circumstances. As an extensive and quick mapping tool, it can support other types of bed material samplings in
757 choosing the sampling locations and their optimal number. Furthermore, it can be used for quickly detecting areas
758 of sedimentation and their extent, as ~~we it was shown~~ in Section 3.2. (e.g., Fig. 12b). This way, it can support
759 decision-making regarding the maintenance of the channel or the bank-infiltrated drinking water production
760 (detecting colmation zones). Fourth, a novel approach was used for the imaging and model training. As the
761 camera-bed distance was constantly changing, the mm/pixel ratio also varied. Hence, no scale was defined for the
762 algorithm beforehand. ~~As we discussed in Section 1., Earlier DL-Deep Learning~~ methods for sediment analysis
763 ~~(e.g., Soloy et al., 2020)~~ all applied fixed camera heights and/or provided scaling for the AI. Furthermore, these
764 studies were based on airborne measurements, mapping the dry zone of the rivers. In an underwater manner, it is
765 extremely challenging to keep a fixed, constant camera height due to the spatially varying riverbed elevations. By
766 avoiding the need for a scale, our method is faster and simpler to use. As a drawback, our method does not
767 reconstruct Hence, it is of major importance that this manuscript introduces a methodology and a Deep Learning
768 ~~algorithm which neglect the need for scaling. This way, the method is faster and easier to build, but also simpler~~
769 ~~to use. Due to this, the method does not reconstruct~~ detailed grainsize distributions, but rather measures the relative
770 portions of the main sediment classes: sand, gravel, cobble. In short, this study showcased a fast bed material
771 mapping tool, with a much denser spatial resolution than the conventional methods, saving up significant
772 resources.

773
774 Originally, beside the three classes of main sediment types introduced in the ~~study-manuscript~~, others were also
775 defined during annotation (e.g., bedrock, clams), but due to class imbalance (i.e., dominance of the three sediment
776 classes), these were not ~~discriminated-adapted~~ successfully. In the future, improving the method through transfer
777 learning (Zamir et al., 2018) using broader dataset and involving other sediment types will be considered. Another
778 option for developing the method is to counter imbalance with the use of so-called weighted cross entropy (see
779 Lu et al., 2019) on the current dataset, which will also be investigated.

780
781 Since the introduced method offers a quick way to provide extensive, spatially dense bed material information of
782 its composition, it can be used to boost the training dataset of predictive, ensemble bagging-based Machine
783 Learning techniques (e.g., Ren et al., 2020) and improve their accuracy. Furthermore, the method can support the
784 implementation of other ~~imaging imagery~~ techniques. For instance, using one of the training videos of this study
785 the authors managed to reconstruct the grain-scale 3D model of a riverbed section with the Structure-from-Motion
786 technique (Ermilov et al., 2020), enabling the quantitative estimation of surface roughness. Underwater field
787 cameras can also be used for monitoring and estimating bedload transport rate (Ermilov et al., 2022) by adapting
788 Large-scale – Particle Image Velocimetry-LS-PIV and the Statistical Background Model approach. This latter
789 videography technique may also be used with moving cameras (e.g., Hayman and Ekhlund, 2003), which enables
790 its adaptation into our method by e.g., detecting bedload movement in the cross-section.

791

792 The statistical representativity of the introduced method, as a surface sampling technique, needs to also be
793 addressed in future work. Following and building upon the experience of conventional, surface sampling
794 procedures (e.g., grid sampling; Diplas, 1988) may prove to be beneficial, where they provided the exact number
795 of gravel particles needed to be included (Wolman, 1954) to satisfy the representativity criteria. Then, using edge-
796 and blob-detection would enable to calculate and compare the number of gravel particles in the images to this
797 value. Furthermore, we intend to apply 2 cameras, with overlapping FOVs for increasing the covered area (and
798 the representativity) during surveys. Besides, it would also improve the accuracy of the Structure-from-Motion
799 technique mentioned earlier.

800 4 Conclusion

801 ~~We introduced a novel, AI-based method for riverbed sediment analysis. The method uses underwater images to~~
802 ~~reconstruct spatial variations in sediment grain sizes. Trained and validated with ~15.000 underwater images~~
803 ~~collected in a section of the Danube in Hungary, we showed that the method can map the riverbed along the~~
804 ~~vessel's route at a high spatial density of approximately 60-100 overlapping sample images per meter. The method~~
805 ~~does not require a scale and thus allows the distance between the camera and the riverbed to vary. In contrast to~~
806 ~~conventional point samples of river-bed substrate, our method provides spatially continuous data, that can be~~
807 ~~further enhanced (e.g., by interpolation) to 2D maps. The method can be applied in studies where dense~~
808 ~~information about river-bed composition is required, such as riverine habitat studies, computational hydro- and~~
809 ~~morphodynamic models, or analyses of river-restoration measures. A novel, artificial intelligence based riverbed~~
810 ~~sediment analysis method has been introduced in this manuscript, which uses underwater images to reconstruct~~
811 ~~the spatial variation of the characteristic sediment classes. The method was trained and validated with a reasonably~~
812 ~~high number (~15000) of images, collected in a large river, in the Hungarian section of the Danube. The main~~
813 ~~novelties of the developed Deep Learning based procedure are the followings: i) underwater images are used, ii)~~
814 ~~the method enables mapping of the riverbed along the measurement vessel's route with very dense spatial~~
815 ~~allocation, iii) cost efficient, iv) works without scaling, i.e., the distance between the camera and the riverbed can~~
816 ~~vary. Consequently, in contrast with conventional pointwise bed sediment analysis methods, this technique is~~
817 ~~robust and capable of providing continuous sediment composition data covering whole river reaches, eventually~~
818 ~~providing the possibility to set up 2D bed material maps. In this way, river reach scale hydromorphological~~
819 ~~assessments can be supported, where the composition of bed surface is of interest, e.g., when performing habitat~~
820 ~~studies, parameterising 2D and 3D computational hydrodynamic and morphodynamic models, or assessing the~~
821 ~~impact of restoration measures.~~

822 **Financial support.** The first author acknowledges the support of the ÚNKP-21-3 New National Excellence
823 Programme of the Ministry for Innovation and Technology, and the National Research, Development and
824 Innovation Fund, Hungary.

825 **Code availability.** The code written and used in this ~~study manuscript~~ is available [here](#).

826 **Data availability.** The dataset and results can be accessed using the following links:
827 [link1](#); [link2](#); [link3](#).

828 **Author contributions.** GB developed the code and carried out the training process. AAE carried out the
829 fieldwork, evaluated the results, did the laboratory analysis, and collaborated with GB in improving the images.
830 SB oversaw and directed the project, while managing the financial- and equipment background.

831 **Competing interest.** The contact author has declared that none of the authors has any competing interest.

832 **Acknowledgements.** The authors would like to thank our students Dávid Koós, Gergely Tikász, Schrott Márton
833 and our technicians István Galgóczy, István Pozsgai, Károly Tóth and András Rehák for fieldwork support.

834 **References**

835 Adams, J.: Gravel Size Analysis from Photographs. *J. Hydraul. Div.*, 1979, 105, 1247–1255.
836 doi/10.1061/JYCEAJ.0005283, 1979.

837
838 Anglin, D. R., Haeseker, S. L., Skalicky, J. J., Schaller, H., Tiffan, K. F., Hatten, J. R., et al.: Effects of Hydropower
839 Operations on Spawning Habitat, Rearing Habitat, and Standing/Entrapment Mortality of Fall Chinook Salmon
840 in the Hanford Reach of the Columbia River. US Fish and Wildlife Service, final Report. Available at:
841 <https://pubs.er.usgs.gov/publication/70179516>, 2006.

842
843 Baranya, S., Fleit, G., Józsa, J., Szalóky, Z., Tóth, B., Czeglédi, I. and Erős, T.: Habitat mapping of riverine fish
844 by means of hydromorphological tools. *Ecohydrology*, Volume 11, Issue 7 e2009. Available at:
845 <https://doi.org/10.1002/eco.2009>, 2018.

846
847 Barnard, P., Rubin, D., Harney, J. and Mustain, N.: Field test comparison of an autocorrelation technique for
848 determining grain size using a digital beachball camera versus traditional methods. *Sedimentary Geology*, 201(1–
849 2): 180–195., 2007.

850
851 Benjankar, R., Tonina, D., Mckean, J.: One-dimensional and two-dimensional hydrodynamic modelling derived
852 flow properties: Impacts on aquatic habitat quality predictions. *Earth Surf. Process. Landf.* 2015, 40, 340–356.

853
854 Benkő, G., Baranya, S., Török, T. G., and Molnár, B.: Folyami mederanyag szemösszetételének vizsgálata Mély
855 Tanulás eljárással drónfelvételek alapján (in English: Analysis of composition of riverbed material with Deep
856 Learning based on drone video footages). *Hidrológiai Közlöny*, 100, 61–69., 2020. Manuscript
857 Breheret, A.: Pixel Annotation Tool. Av. at: <https://github.com/abreheret/PixelAnnotationTool>, 2017.

858
859 Bunte, K. and Abt, S. R.: Sampling Surface and Subsurface Particle-Size Distributions in Wadable Gravel- and
860 Cobble-Bed Streams for Analyses in Sediment Transport, Hydraulics, and Streambed Monitoring; General
861 Technical Report (GTR), U.S. Department of Agriculture, Forest Service, Rocky Mountain Research Station: Fort
862 Collins, CO, USA, 2001.

863
864
865 Buscombe, D. and Masselink, G.: Grain size information from the statistical properties of digital images of
866 sediment. *Sedimentology*, 56, 421–438. doi/10.1111/j.1365-3091.2008.00977.x, 2008.

867
868 Buscombe, D.: Transferable wavelet method for grain-size distribution from images of sediment surfaces and thin
869 sections, and other natural granular patterns. *Sedimentology*, 60 1709–1732., 2013.

870
871 Buscombe, D., Grams, P. and Kaplinski, M.: Characterizing riverbed sediment using high-frequency acoustics: 1.
872 Spectral properties of scattering. *Journal of Geophysical Research: Earth Surface*, doi: 10.1002/2014JF003189,
873 119:12, (2674-2691), 2014a.

874
875 Buscombe, D., Grams, P. and Kaplinski, M.: Characterizing riverbed sediment using high-frequency acoustics: 2.
876 Scattering signatures of Colorado Riverbed sediment in Marble and Grand Canyons. *Journal of Geophysical
877 Research: Earth Surface*, doi/full/10.1002/2014JF003191, 119:12, (2674-2691), 2014b.

878

879 Buscombe, D. and Ritchie, A. C.: Landscape Classification with Deep Neural Networks. *Geosciences*, 8, 244.
880 Available at: <https://doi.org/10.3390/geosciences8070244> , 2018.
881

882 Buscombe, D.: SediNet: a configurable deep learning model for mixed qualitative and quantitative optical
883 granulometry optical granulometry. *Earth Surface Processes and Landforms*, 45, 638-651. DOI:
884 10.1002/esp.4760, 2020.
885

886

887 Chandler, J., Lane, S. N. and Ashmore, P.: Measuring river-bed and flume morphology and parameterising bed
888 roughness with a KODAK DCS460 digital camera. *International Archives of Photogrammetry and Remote*
889 *Sensing*, Vol. XXXIII, Part B7., 2000.
890

891 Chen, C., Zhang, P., Zhang, H., Dai, J., Yi, Y., Zhang, H. and Zhang, Y.: Deep Learning on Computational-
892 Resource-Limited Platforms: A Survey. Volume 2020, Article ID 8454327. Available at:
893 <https://doi.org/10.1155/2020/8454327>, 2020.
894

895 Chen, L., Zhu, Y., Isola, P., Papandreou, G., Schroff, F. and Adam, H.: Encoder-Decoder with Atrous Separable
896 Convolution for Semantic Image Segmentation. *Proceedings of the European conference on computer vision*
897 *(ECCV)* (pp. 801-818). <https://arxiv.org/abs/1802.02611>., 2018.
898

899 Cheng, D., Li, X., Li, W. H., Lu, C., Li, F., Zhao, H. and Zheng, W. S.: Large-Scale Visible Watermark Detection
900 and Removal with Deep Convolutional Networks. In book: *Pattern Recognition and Computer Vision. First*
901 *Chinese Conference, PRCV, Guangzhou, China, Proceedings, Part III*. DOI: 10.1007/978-3-030-03338-5_3,
902 2018.
903

904 Cheng, Z., and Liu, H.: Digital grain-size analysis based on autocorrelation algorithm. *Sedimentary Geology*, 327,
905 21-31. Available at: <https://doi.org/10.1016/j.sedgeo.2015.07.008>, 2015.
906

907 Chezar, H. and Rubin, D. M.: Underwater Microscope System. United States Patent Office, The United States of
908 America as represented by the Secretary of the Interior, US Patent No. 6,680,795 B2., 2004.
909

910 Church, M. A., McLean, D. G., and Wolcott, J. F.: Sediments transport in Gravel Bed Rivers. Chap.: *Riverbed*
911 *Gravels: Sampling and Analysis*. John Wiley and Sons, New York, 43–88, 1987.
912

913 Cui, G., Su, X., Liu, Y., & Zheng, S.: Effect of riverbed sediment flushing and clogging on river-water infiltration
914 rate: a case study in the Second Songhua River, Northeast China. *Hydrogeology Journal*, 29(2), 551–565.
915 <https://doi.org/10.1007/s10040-020-02218-7>, 2021.
916

917 Delong, M. D. and Brusven, M. A.: Classification and spatial mapping of riparian habitat with applications toward
918 management of streams impacted by nonpoint source pollution. *Environmental Management*, 15:565-571. DOI:
919 10.1007/BF02394745, 1991.
920

921 Detert, M. and Weitbrecht, V.: User guide to gravelometric image analysis by BASEGRAIN. In *Advances in*
922 *Science and Research*; Fukuoka, S., Nakagawa, H., Sumi, T., Zhang, H., Eds.; Taylor and Francis Group: London,
923 UK, 2013; pp. 1789–1795. ISBN 978-1-138-00062-9., 2013.
924

925 Diplas, P.: Sampling Techniques for Gravel Sized Sediments. *Journal of Hydraulic Engineering*. DOI:
926 10.1061/(ASCE)0733-9429(1988)114:5(484), 1988.
927

928 Ermilov, A.A., Baranya, S. and Török, G.T.: Image-Based Bed Material Mapping of a Large River. *Water*, 12,
929 916. Available at: <https://doi.org/10.3390/w12030916>, 2020.
930

931 Ermilov, A. A., Fleit, G., Conevski, S., Guerrero, M., Baranya, S., & Rütther, N.: Bedload transport analysis using
932 image processing techniques. *ACTA GEOPHYSICA*, 1895-6572 1895-7455. [http://doi.org/10.1007/s11600-022-](http://doi.org/10.1007/s11600-022-00791-x)
933 [00791-x](http://doi.org/10.1007/s11600-022-00791-x), 2022.
934

935 Fehr, R.: Einfache Bestimmung der Korngrößenverteilung von Geschiebematerial mit Hilfe der
936 Linienzahlanalyse (In English: Simple detection of grain size distribution of sediment material using line-count
937 analysis). *Schweizer Ing. und Archit.*, 105, 1104–1109., 1987.
938

939 Ferdowsi, B., Ortiz, C. P., Houssais, M., & Jerolmack, D. J. (2017). Riverbed armouring as a granular segregation
940 phenomenon. *Nature Communications* 2017 8:1, 8(1), 1–10. <https://doi.org/10.1038/s41467-017-01681-3>
941

942 Fetzer, J., Holzner, M., Plötze, M. and Furrer, G.: Clogging of an Alpine streambed by silt-sized particles –
943 Insights from laboratory and field experiments. *Water Research*, Volume 126, Pages 60-69.
944 <https://doi.org/10.1016/j.watres.2017.09.015>, 2017.
945

946 Geist, D. R., Jones, J., Murray, C. J. and Dauble, D. D.: Suitability criteria analyzed at the spatial scale of redd
947 clusters improved estimates of fall chinook salmon (*Oncorhynchus tshawytscha*) spawning habitat use in the
948 Hanford Reach, Columbia River. *Canadian Journal of Fisheries and Aquatic Sciences*, 57: 1636-1646., 2000.
949

950 Gilcher, M. and Udelhoven, T.: Field Geometry and the Spatial and Temporal Generalization of Crop
951 Classification Algorithms—A Randomized Approach to Compare Pixel Based and Convolution Based Methods.
952 *Remote Sens.*, 13, 775., 2021.
953

954 GOPRO Hero 4 Silver: User Manual. Available at: [https://gopro.com/content/dam/help/hero4-](https://gopro.com/content/dam/help/hero4-silver/manuals/UM_H4Silver_ENG_REVA_WEB.pdf)
955 [silver/manuals/UM_H4Silver_ENG_REVA_WEB.pdf](https://gopro.com/content/dam/help/hero4-silver/manuals/UM_H4Silver_ENG_REVA_WEB.pdf), 2014.
956

957 GOPRO Hero 7 Black: User Manual. Available at: [https://gopro.com/content/dam/help/hero7-](https://gopro.com/content/dam/help/hero7-black/manuals/HERO7Black_UM_ENG_REVA.pdf)
958 [black/manuals/HERO7Black_UM_ENG_REVA.pdf](https://gopro.com/content/dam/help/hero7-black/manuals/HERO7Black_UM_ENG_REVA.pdf), 2018.
959

960 Graham, D. J., Reid, I. and Rice, S. P.: Automated sizing of coarse-grained sediments: image-processing
961 procedures. *Mathematical Geology*, 37, 1–28. <https://doi.org/10.1007/s11004-005-8745-x>, 2005.
962

963 Graham, D. J. Rollet, A.J., Piégay, H. and Rice, S. P.: Maximizing the accuracy of image-based surface sediment
964 sampling techniques. *Water Resour. Res.*, 46, W02508. [https://doi.org/](https://doi.org/10.1029/2008WR006940)
965 [10.1029/2008WR006940](https://doi.org/10.1029/2008WR006940), 2010.
966

967 Grams, P. E., Topping, D. J., Schmidt, J. C., Hazel, J. E. and Kaplinski, M.: Linking morphodynamic response
968 with sediment mass balance on the Colorado River in Marble Canyon: Issues of scale, geomorphic setting, and
969 sampling design, *J. Geophys. Res. Earth Surf.*, 118, 361–381, doi:10.1002/jgrf.20050., 2013.
970

971 Guerit, L., Barrier, L., Liu, Y., Narteau, C., Lajeunesse, E., Gayer, E., Métivier, F.: Uniform grain-size distribution
972 in the active layer of a shallow, gravel-bedded, braided river (the Urumqi River, China) and implications for paleo-
973 hydrology. *Earth Surface Dynamics*. 6. 1011-1021. DOI: 10.5194/esurf-6-1011-2018., 2018.
974

975 Guerrero, M., Rüther, N., Szupiany, R., Haun, S., Baranya, S. and Latosinski, F.: The Acoustic Properties of
976 Suspended Sediment in Large Rivers: Consequences on ADCP Methods Applicability. *Water*, 8, 13;
977 doi:10.3390/w8010013, 2016.
978

979 Haddadchi, A., Booker, D.J. and Measures, R.J.: Predicting riverbed substrate cover proportions across New
980 Zealand. *Catena*, Volume 163, pp. 130-146. Available at: <https://doi.org/10.1016/j.catena.2017.12.014>, 2018.
981

982 Hayman, E., Eklundh, J.: Statistical Background Subtraction for a Mobile Observer. *Proceedings of the Ninth*
983 *IEEE International Conference on Computer Vision (ICCV 2003) 2-Volume Set 0–7695–1950–4/03*, 2003.
984

985 He, F., Liu, T., Tao, D.: Control batch size and learning rate to generalize well: theoretical and empirical evidence.
986 *Neural Information Processing Systems*, 2019.
987

988 Ibbeken, H., and Schleyer, R.: Photo-sieving: A method for grain-size analysis of coarse-grained, unconsolidated
989 bedding surfaces. *Earth Surf. Process. Landforms*, 11, 59–77. Available at:
990 <https://doi.org/10.1002/esp.3290110108>, 1986.
991

992 Ighathinathane, C., Melin, S., Sokhansanj, S., Bi, X., Lim, C. J., Pordesimo, L. O. and Columbus, E. P.: Machine
993 vision based particle size and size distribution determination of airborne dust particles of wood and bark pellets.
994 *Powder Technol.*, 196, 202–212. Available at: <https://doi.org/10.1016/j.powtec.2009.07.024>, 2009.
995

996 Kellerhals, R. and Bray, D. I.: Sampling Procedures for Coarse Fluvial Sediments. *J. Hydraul. Div.*, 97, 1165–
997 1180., 1971.
998

999 Kim, H., Han, J. and Han, T. Y.: Machine vision-driven automatic recognition of particle size and morphology in
1000 SEM images. *Nanoscale*, 12, 19461–19469. Available at: <https://doi.org/10.1039/D0NR04140H>, 2020.
1001
1002 Kinsman, N.: Single-Beam Bathymetry Data Collected in Shallow-Water Areas near Gambell, Golovin, Hooper
1003 Bay, Savoonga, Shishmaref, and Wales, Alaska 2012–2013; Department of Natural Resources. Division of
1004 Geological & Geophysical Surveys: Fairbanks, AK, USA, 2015.
1005
1006 Le, Q. V.: Building high-level features using large scale unsupervised learning. In Proceedings of the 2013 IEEE
1007 International Conference on Acoustics, Speech and Signal Processing, Vancouver, BC, Canada, pp. 8595–8598.,
1008 2013.
1009
1010 Leopold, L. B.: An Improved Method for Size Distribution of Stream Bed Gravel. *Water Resour. Res.*, 6, 1357–
1011 1366. <https://doi.org/10.1029/WR006i005p01357>, 1970.
1012
1013 Limare, A., Tal, M., Reitz, M. D., Lajeunesse, E., and Métivier, F.: Optical method for measuring bed topography
1014 and flow depth in an experimental flume. *Solid Earth*, 2, 143–154, <https://doi.org/10.5194/se-2-143-2011>., 2011.
1015
1016 Lowe, D. G.: Distinctive Image Features from Scale-Invariant Keypoints. *International Journal of Computer*
1017 *Vision*, 60, pages 91–110, 2004.
1018
1019 Lu, S., Gao, F., Piao, Ch. and Ma, Y.: Dynamic Weighted Cross Entropy for Semantic Segmentation with
1020 Extremely Imbalanced Data. 2019 International Conference on Artificial Intelligence and Advanced
1021 Manufacturing (AIAM). doi: 10.1109/AIAM48774.2019.00053, 2019.
1022
1023 Mueller D. S., Wagner, Ch. R.: Measuring Discharge with Acoustic Doppler Current Profilers from a Moving
1024 Boat. USGS, Chapter 22 of Book 3, Section A. <https://pubs.usgs.gov/tm/3a22/>, 2009.
1025
1026 Muñoz-Mas, R., Sánchez-Hernández, J., McClain, M. E., Tamatamah, R., Mukama, S. C., & Martínez-Capel, F.:
1027 Investigating the influence of habitat structure and hydraulics on tropical macroinvertebrate communities.
1028 *Ecohydrology and Hydrobiology*, 19(3), 339–350. <https://doi.org/10.1016/j.ecohyd.2018.07.005>, 2019.
1029
1030 Mueller D. S., Wagner, Ch. R.: Measuring discharge with acoustic Doppler current profilers from a moving boat,
1031 version 2.0. [https://www.researchgate.net/publication/284587353_Measuring_discharge_with_acoustic_-_](https://www.researchgate.net/publication/284587353_Measuring_discharge_with_acoustic_-_Doppler_current_profilers_from_a_moving_boat)
1032 [Doppler current profilers from a moving boat](https://www.researchgate.net/publication/284587353_Measuring_discharge_with_acoustic_-_Doppler_current_profilers_from_a_moving_boat), 2013.
1033
1034 Muste, M., Baranya, S., Tsubaki, R., Kim, D., Ho, H., Tsai, H. and Law, D.: Acoustic mapping velocimetry. *Water*
1035 *Resour. Res.*, 52, 4132–4150, doi:10.1002/2015WR018354., 2016.
1036
1037 Obodovskyi, O., Habel, M., Szatten, D., Rozlach, Z., Babiński, Z., Maerker, M.: Assessment of the Dnieper
1038 Alluvial Riverbed Stability Affected by Intervention Discharge Downstream of Kaniv Dam. *Water*, 12(4):1104.
1039 <https://doi.org/10.3390/w12041104>, 2020.
1040
1041 Padilla, R., Netto, S. M. and da Silva, E. A. B.: A Survey on Performance Metrics for Object-Detection
1042 Algorithms. Conference: 2020 International Conference on Systems, Signals and Image Processing (IWSSIP).
1043 DOI: 10.1109/IWSSIP48289.2020, 2020.
1044
1045 Perez, L. and Wang, J.: The Effectiveness of Data Augmentation in Image Classification using Deep Learning.
1046 arXiv preprint arXiv:1712.04621. Av. at: <https://arxiv.org/abs/1712.04621>. 2017., 2017.
1047
1048 Purinton, B. and Bookhagen, B.: Introducing PebbleCounts: A grain-sizing tool for photo surveys of dynamic
1049 gravel-bed rivers. *Earth Surf. Dyn.*, 7, 859–877. <https://doi.org/10.5194/esurf-7-859-2019>, 2019.
1050
1051 Rákóczi, L.: Selective erosion of noncohesive bed materials. *Geografiska Annaler. Series A, Physical Geography*,
1052 Vol. 69, No. 1, pp. 29-35. <https://doi.org/10.2307/521364>, 1987.
1053
1054 Rákóczi, L.: Identification of river channel areas inclined for colmation, based on the analysis of bed material.
1055 *Vízügyi Közlemények*, LXXIX., chapter 3., 1997.
1056

1057 Rahman, M. A. and Wang, Y.: Optimizing Intersection-Over-Union in Deep Neural Networks for Image
1058 Segmentation. In: Bebis G. et al. (eds) *Advances in Visual Computing. ISVC 2016. Lecture Notes in Computer*
1059 *Science*, vol 10072. Springer, Cham. https://doi.org/10.1007/978-3-319-50835-1_22, 2016.

1060

1061 RD Instruments – Acoustic Doppler Current Profilers – Application Note: https://www.commtec.com/library/Technical_Manuscripts/RDI/FSA-004%20Model.pdf, 1999.

1062

1063

1064 Rice, S. and Church, M.: Grain size along two gravel-bed rivers: Statistical variation, spatial pattern and
1065 sedimentary links. *Earth Surf. Process. Landf.*, 23, 345–363., 1998.

1066

1067 Ren, H., Hou, Z., Duan, Z., Song, X., Perkins, W.A., Richmond, M. C., Arntzen, E. V. and Scheibe, T. D.: Spatial
1068 Mapping of Riverbed Grain-Size Distribution Using Machine Learning. *Front. Water*, 2:551627. doi:
1069 10.3389/frwa.2020.551627, 2020.

1070

1071 Rozniak, A., Schindler, K., Wegner, J. D. and Lang, N.: Drone images and Deep Learning for river monitoring in
1072 Switzerland. Semester project. Institute of Geodesy and Photogrammetry, Project, Swiss Federal Institute of
1073 Technology (ETH) Zurich, 2019.

1074

1075 Rubin, D. M.: A simple autocorrelation algorithm for determining grain-size from digital images of sediment. *J.*
1076 *Sed. Res.*, 74, 160–165., 2004.

1077

1078 Rubin, D. M., Chezar, H., Harney, J. N., Topping, D. J., Melis, T. S., Sherwood, C. R.: Underwater microscope
1079 for measuring spatial and temporal changes in bed-sediment grain size. *Sedimentary Geology*, Volume 202, Issue
1080 3, Pages 402-408, <https://doi.org/10.1016/j.sedgeo.2007.03.020>, 2007.

1081

1082 Scheder, C., Lerchegger, B., Flödl, P., Csar, D., Gumpinger, C. and Hauer, C.: Riverbed stability versus clogged
1083 interstitial: Depth-dependent accumulation of substances in freshwater pearl mussel (*Margaritifera margaritifera*
1084 L.) habitats in Austrian streams as a function of hydromorphological parameters. *Limnologica*, Volume 50,
1085 January 2015, Pages 29-39. <https://doi.org/10.1016/j.limno.2014.08.003>, 2015.

1086

1087 Shields, F. D., Jr. and Rigby, J. R.: River habitat quality from river velocities measured using acoustic Doppler
1088 current profiler. *Environ. Manage.*; 36(4):565-75. doi: 10.1007/s00267-004-0292-6., 2005.

1089

1090 Shields, F. D. Jr.: Aquatic Habitat Bottom Classification Using ADCP. *Journal of Hydraulic Engineering*, Vol.
1091 136, Issue 5, 2010.

1092

1093 Sime, L. C. and Ferguson, R. I.: Information on grain-sizes in gravel bed rivers by automated image analysis. *J.*
1094 *Sed. Res.*, 73, 630–636., 2003.

1095

1096 Simpson, M. R.: Discharge Measurements Using a Broad-Band Acoustic Doppler Current Profiler. USGS, Open-
1097 File Report 01-1, <https://pubs.usgs.gov/of/2001/ofr0101/>, 2002.

1098

1099 Singer, M. B.: A new sampler for extracting bed material sediment from sand and gravel beds in navigable rivers.
1100 *Earth Surface Processes and Landforms* 33(14):2277 – 2284 DOI: 10.1002/esp.1661, 2008.

1101

1102 Soloy, A., Turki, I., Fournier, M., Costa, S., Peuziat, B. and Lecoq, N.: A Deep Learning-Based Method for
1103 Quantifying and Mapping the Grain Size on Pebble Beaches. *Remote Sens.*, 12, 3659, doi:10.3390/rs12213659,
1104 2020.

1105

1106 Staudt, F., Mullarney, J. C., Pilditch, C. A. and Huhn, K.: Effects of grain-size distribution and shape on sediment
1107 bed stability, near-bed flow and bed microstructure. *Earth Surface Processes and Landforms*, 44(5). DOI:
1108 10.1002/esp.4559, 2018.

1109

1110 Sun, Z., Zheng, H. and Sun, L.: Analysis on the Characteristics of Bed Materials in the Jinghong Reservoir on the
1111 Lancang River. *Sustainability*, 13, 6874. <https://doi.org/10.3390/su13126874>, 2021.

1112

1113 Takechi, H., Aragaki, S. and Irie, M.: Differentiation of River Sediments Fractions in UAV Aerial Images by
1114 Convolution Neural Network. *Remote Sens.*, 13, 3188. <https://doi.org/10.3390/rs13163188>, 2021.

1115

1116 Taravat, A., Wagner, M. P., Bonifacio, R. and Petit, D.: Advanced Fully Convolutional Networks for Agricultural
1117 Field Boundary Detection. *Remote Sens.*, 13, 722., 2021.

1118

1119 Török, G. T., Baranya, S. (2017) Morphological Investigation of a Critical Reach of the Upper Hungarian Danube.
1120 *Periodica Polytechnica Civil Engineering*. 61(4), pp. 752–761. <https://doi.org/10.3311/PPci.10530>, 2017.

1121

1122 USDA: Guidelines for Sampling Bed Material. Technical Supplement 13A, 2007.

1123

1124 Vanoni, V. A. and Hwang, L. S.: Relation between Bed Forms and Friction in Streams. *J. Hydraulics Division.*,
1125 93 (3), 121–144. doi:10.1061/JYCEAJ.0001607, 1967.

1126

1127 Verdú, J. M., Batalla, R. J. and Martínez-Casanovas, J. A.: High-resolution grain-size characterisation of gravel
1128 bars using imagery analysis and geo-statistics. *Geomorphology*, 72, 73–93., 2005.

1129

1130 Warrick, J. A., Rubin, D. M., Ruggiero, P., Harney, J. N., Draut, A. E. and Buscombe, D.: Cobble cam: Grain-
1131 size measurements of sand to boulder from digital photographs and autocorrelation analyses. *Earth Surf. Process*
1132 *Landf.*, 34, 1811–1821. <https://doi.org/10.1002/esp.1877>, 2009.

1133

1134 Wilcock, P. R.: Persistence of armor layers in gravel-bed streams. *Hydrology and Land Surface Studies*.
1135 <https://doi.org/10.1029/2004GL021772>, 2005.

1136

1137 Wolcott, J. F., Church, M.: Strategies for sampling spatially heterogeneous phenomena: The example of river
1138 gravels. *Journal of Sedimentary Research*. v. 61, no. 4, p. 534–543, 1991.

1139

1140 Wolman, M. G.: Method of sampling coarse river bed material. *Trans. Am., Geophysical Union*, 35(6), 951-956.
1141

1142 WMO: Measurement of river sediments: prepared by the Rapporteur on Sediment Transport of the Commission
1143 for Hydrology. Report, World Meteorological Organization - No. 561, Operational hydrology report (OHR)- No.
1144 16, 1981.

1145

1146 Xiao, Y., Li, W., & Yang, S.: Hydrodynamic-sediment transport response to waterway depth in the Three Gorges
1147 Reservoir, China. *Arabian Journal of Geosciences*, 14(775). <https://doi.org/10.1007/s12517-021-07090-7/Published>, 2021.

1148

1149

1150 Yang, F., Yi, M., Cai, Y., Blasch, E., Sullivan, N., Sheaff, C., Chen, G. and Ling, H.: Multitask Assessment of
1151 Roads and Vehicles Network (MARVN). *Proceedings Volume 10641, Sensors and Systems for Space*
1152 *Applications XI*, 106410D, <https://doi.org/10.1117/12.2305972>, 2018.

1153

1154 You, K., Long, M., Wang, J., Jordan M.I.: How Does Learning Rate Decay Help Modern Neural Networks?
1155 <https://doi.org/10.48550/arXiv.1908.01878>, 2019.

1156

1157 Yu, L., Wang, S. and Lai, K.K.: Data Preparation in Neural Network Data Analysis. In book: *Foreign-Exchange-*
1158 *Rate Forecasting with Artificial Neural Networks*. DOI: 10.1007/978-0-387-71720-3_3, 2007.

1159

1160 Zamir, A. R., Sax, A., Shen, W., Guibas, L., Malik, J. and Savarese, S.: Taskonomy: Disentangling Task Transfer
1161 Learning. In *Proceedings of the 2018 IEEE/CVF Conf. on Computer Vision and Pattern Recognition*, Salt Lake
1162 City, UT, USA, pp. 3712–3722. doi: 10.1109/CVPR.2018.00391, 2018.

1163

1164 Zhang, Q., Shi, Y., Chen, Z. and Jiang, T.: ADCP measured flow current of the middle-lower Changjiang River
1165 channel. *Front. Earth Sci., China* 2, 1–9. <https://doi.org/10.1007/s11707-008-0016-y>, 2008.

1166

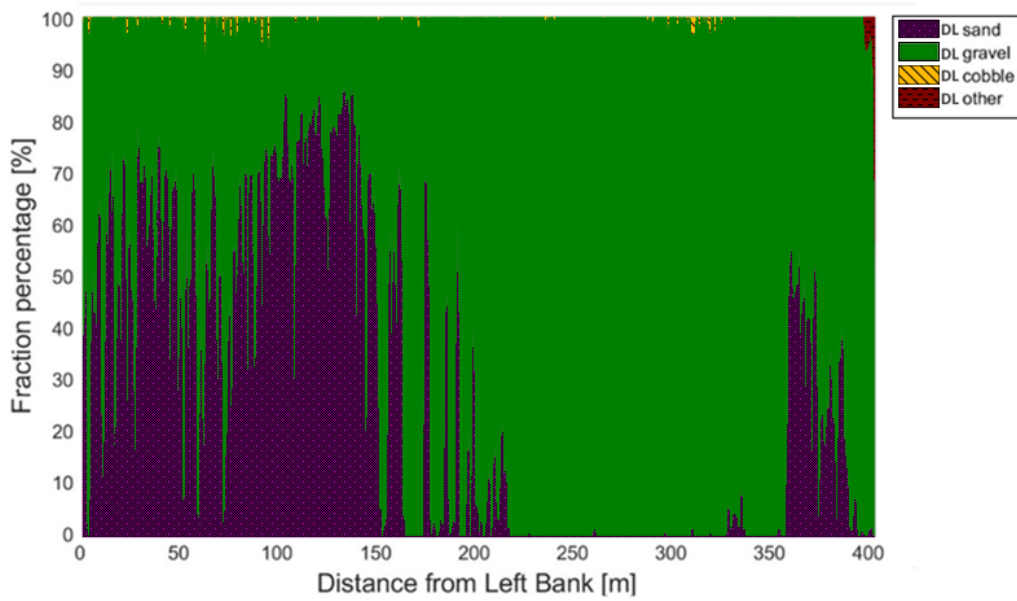
1167 Zhou, Y., Lu, J., Jin, Z., Li, Y., Gao, Y., Liu, Y. and Chen, P.: Experimental Study on the Riverbed Coarsening
1168 Process and Changes in the Flow Structure and Resistance in the Gravel Riverbed Downstream of Dams. *Front.*
1169 *Environ. Sci.*, <https://doi.org/10.3389/fenvs.2021.611668>, 2021.

1170

1171 Zhu, J., Park, T., Isola, P. and Efros, A. A.: Unpaired Image-to-Image Translation using Cycle-Consistent
1172 Adversarial Networks. *arxiv*, <https://arxiv.org/abs/1703.10593>, 2020.

1173 Appendix

1174 Appendix A Site A - Section A – II



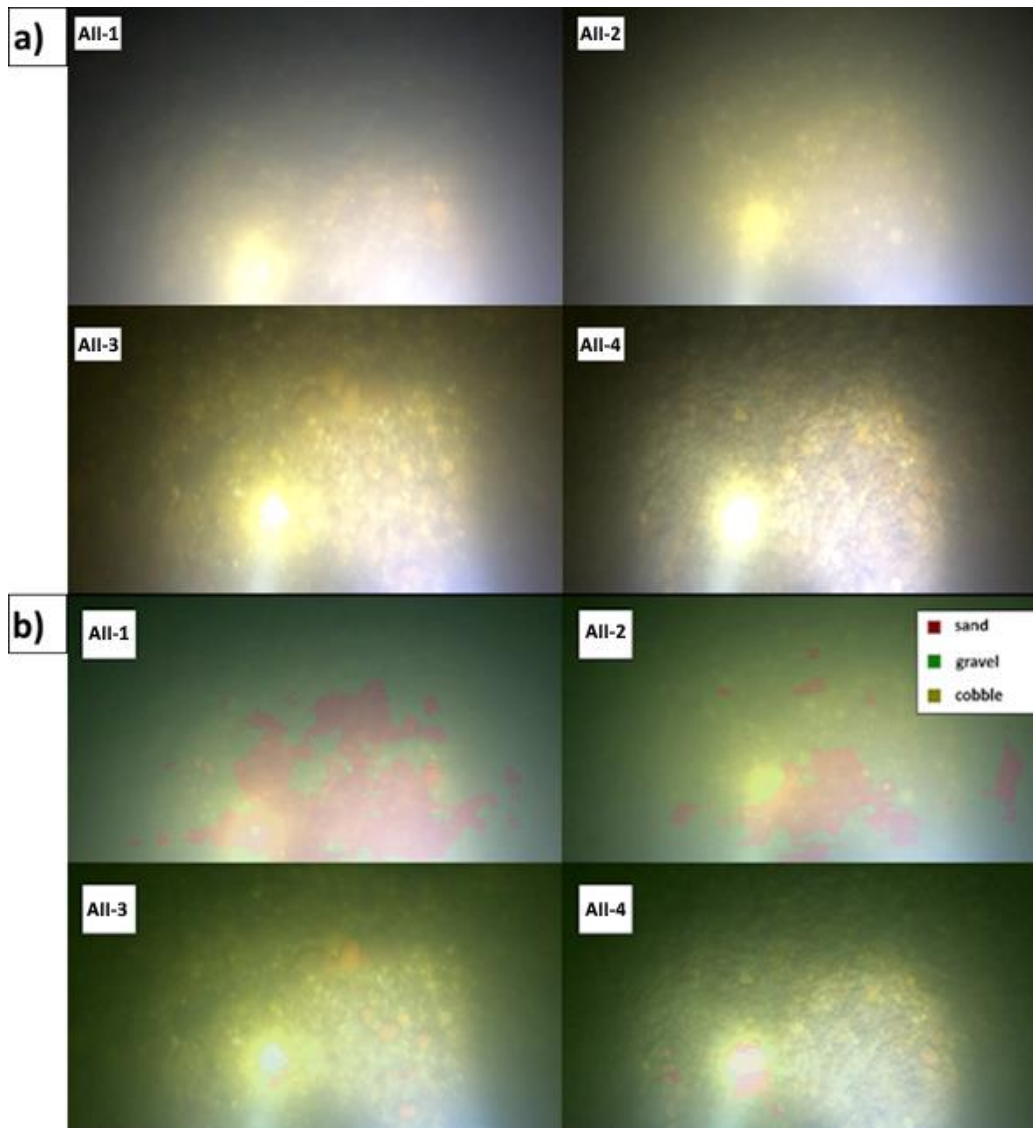
1175 Figure A1: The sediment fraction percentage results of every image, analysed by the DL algorithm along Section A -
1176 II. While the trends are apparent, the sensitivity of the method at its current state can be observed. DL result before
1177 applying moving-averaging.
1178

1179



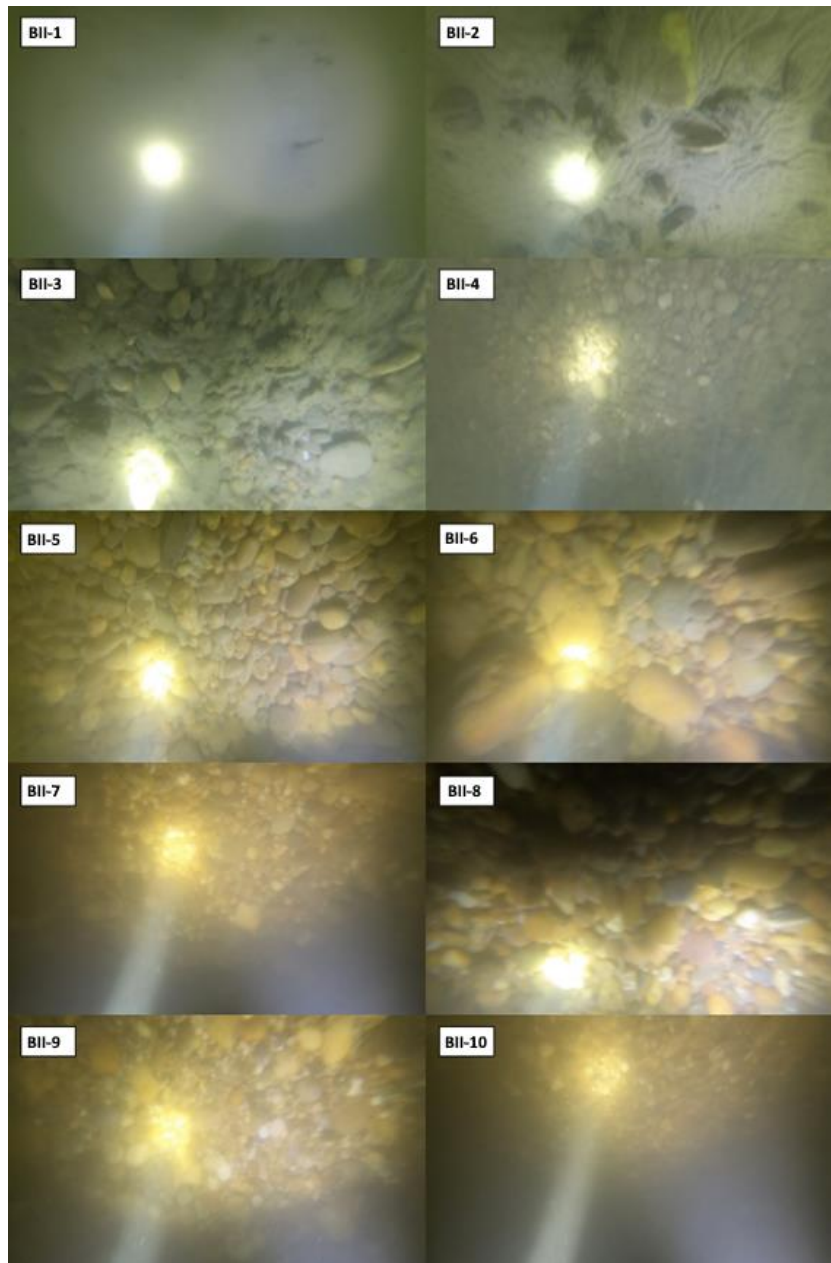
1180 Figure A2: Images of bed armouring, taken during our surveys in the Upper section of the Hungarian Danube. We
1181 broke the surface armour to showcase the presence of the underlying finer fractions.
1182

1183

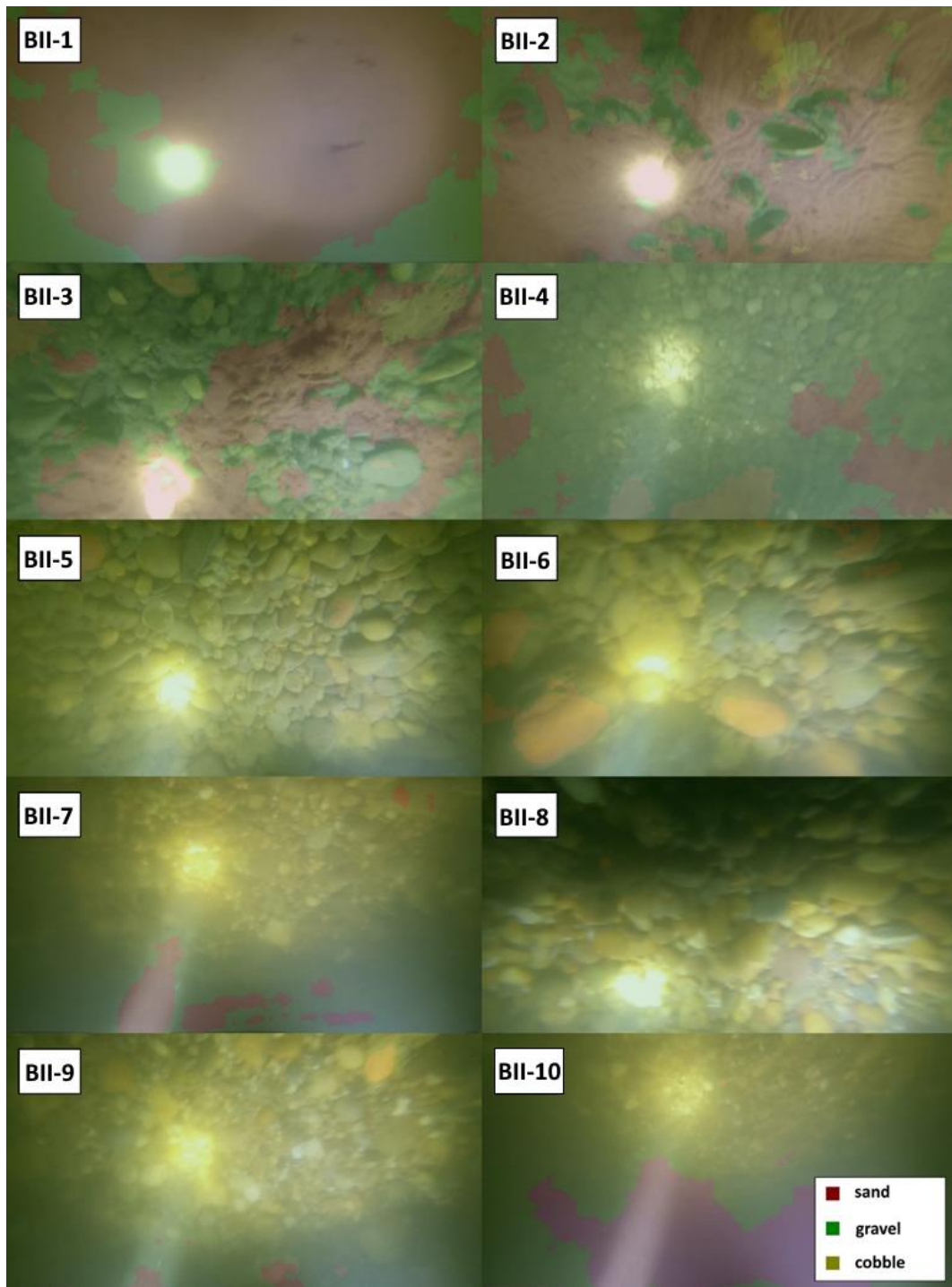


1184
 1185
 1186

Figure A3: a) Riverbed video images at the sampling points in Section A - II. b) Riverbed video images overlapped with their raw, DL detection result, at the sampling points in Section A - II.



1188
1189 Figure B1: Riverbed video images at the sampling points in Section B - II.
1190



1191

1192

1193

Figure B2: Riverbed video images overlapped with their raw, DL detection result, at the sampling points in Section B - II.

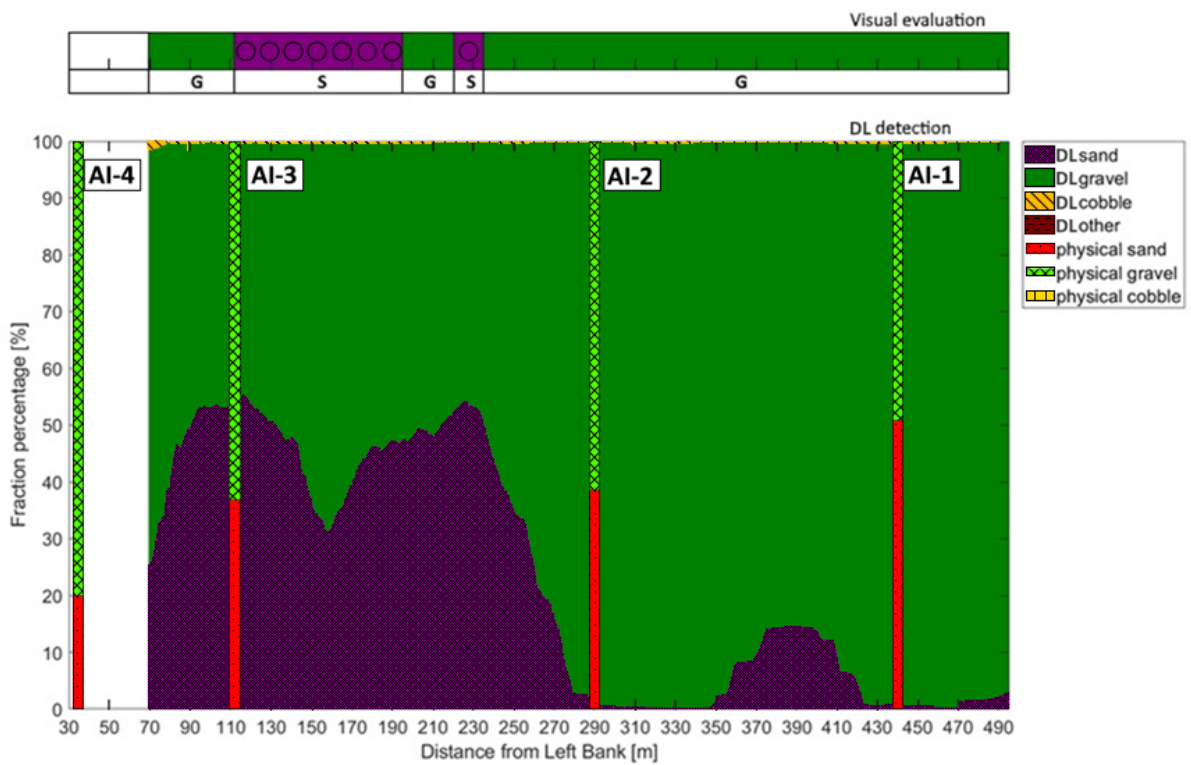
1194

1195 Appendix C Site A - Section A – I



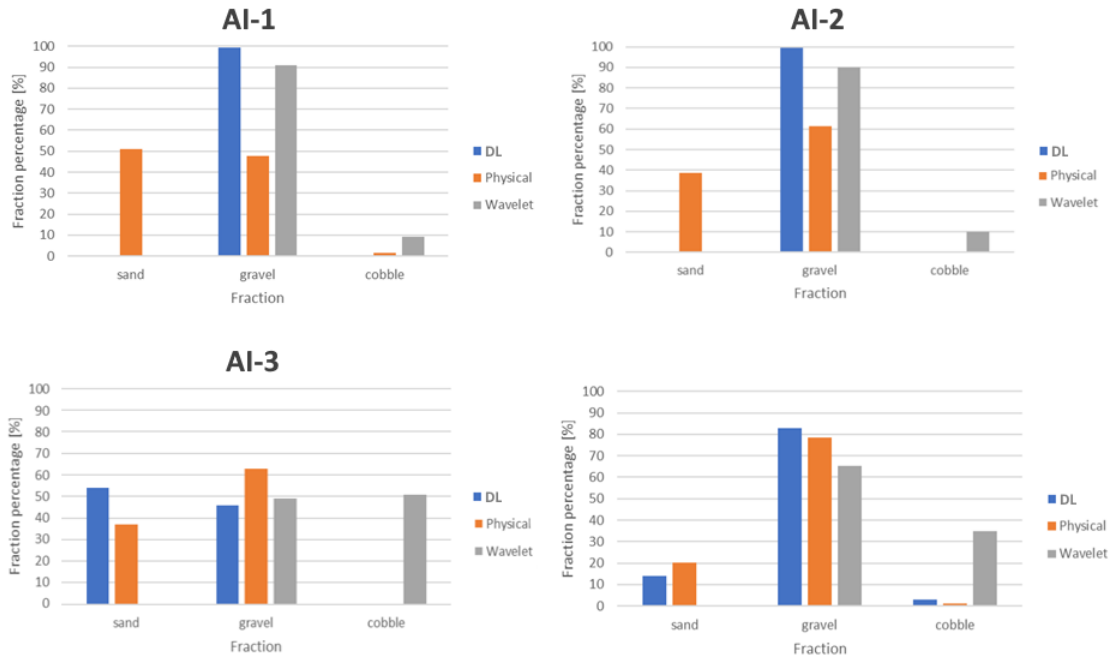
1196 Figure C1: The path of the vessel and camera in Section A - I, Site A. The polyline is coloured based on the sediment
 1197 seen during visual evaluation of the video. Yellow markers are the locations of physical bed material samplings. (Map
 1198 created with Google Earth Pro)
 1199

1200



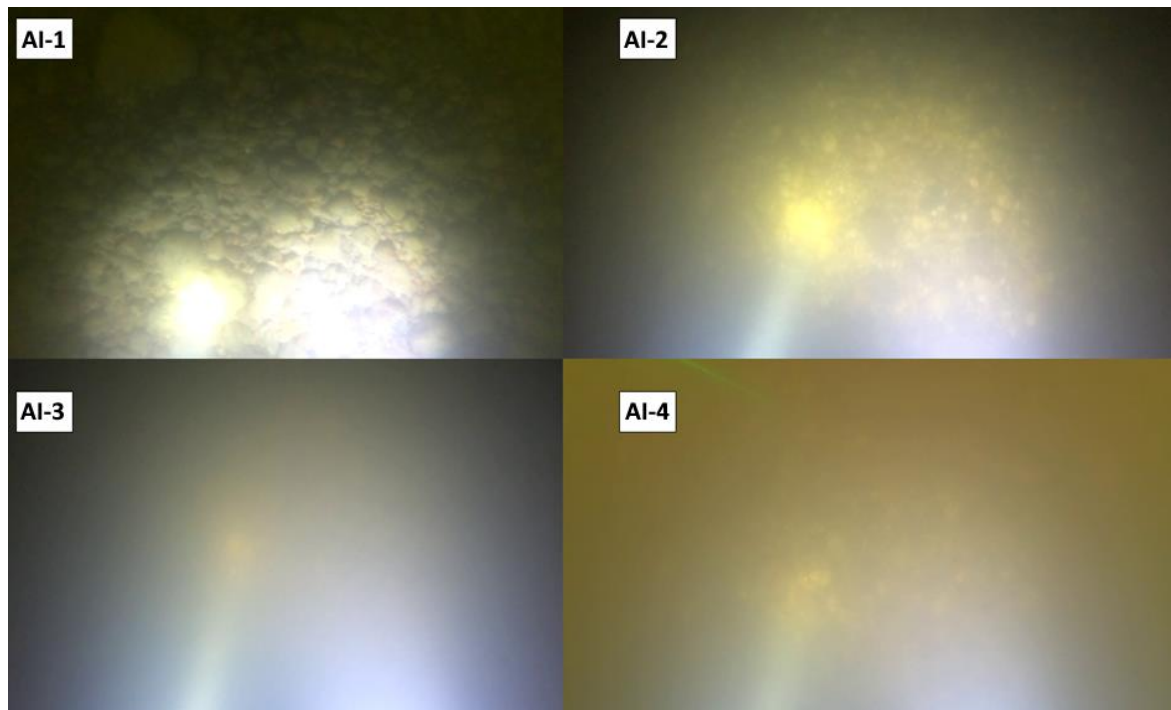
1201 Figure C2: Sediment fraction percentages in Section A - I, recognised by the AI. The visual evaluation included two
 1202 classes: gravel – G, sand – S). The fractions of the physical samples are shown as verticals.
 1203

1204



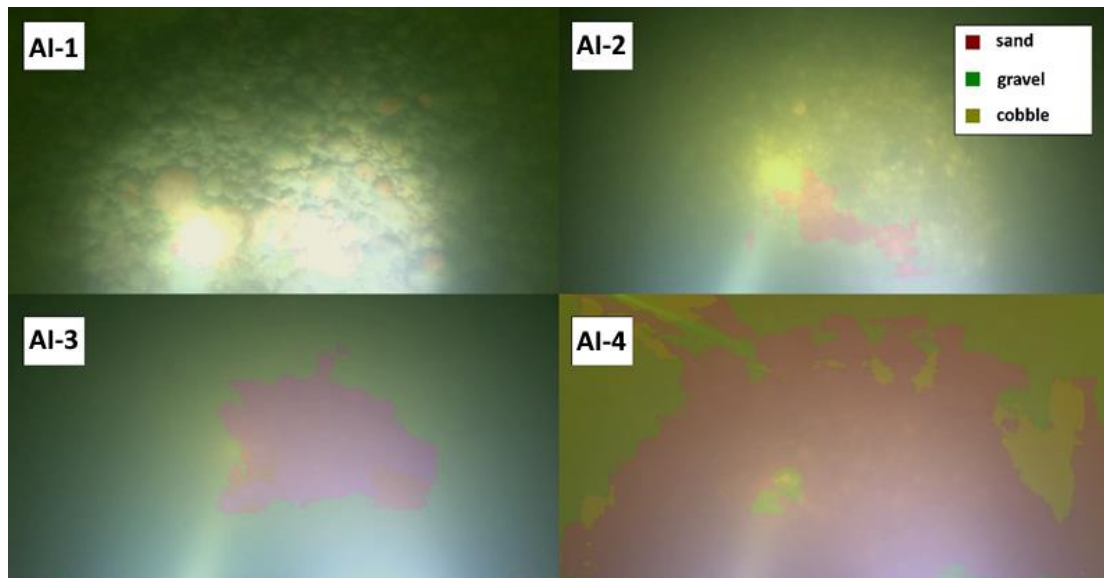
1205
1206
1207

Figure C3: Comparison of sediment fraction % at the sampling locations from the moving-averaged DL detection, conventional sieving and the wavelet-based image processing method. Section A - I.



1208
1209
1210

Figure C4: Riverbed video images at the sampling points in Section A - I.



1211

1212

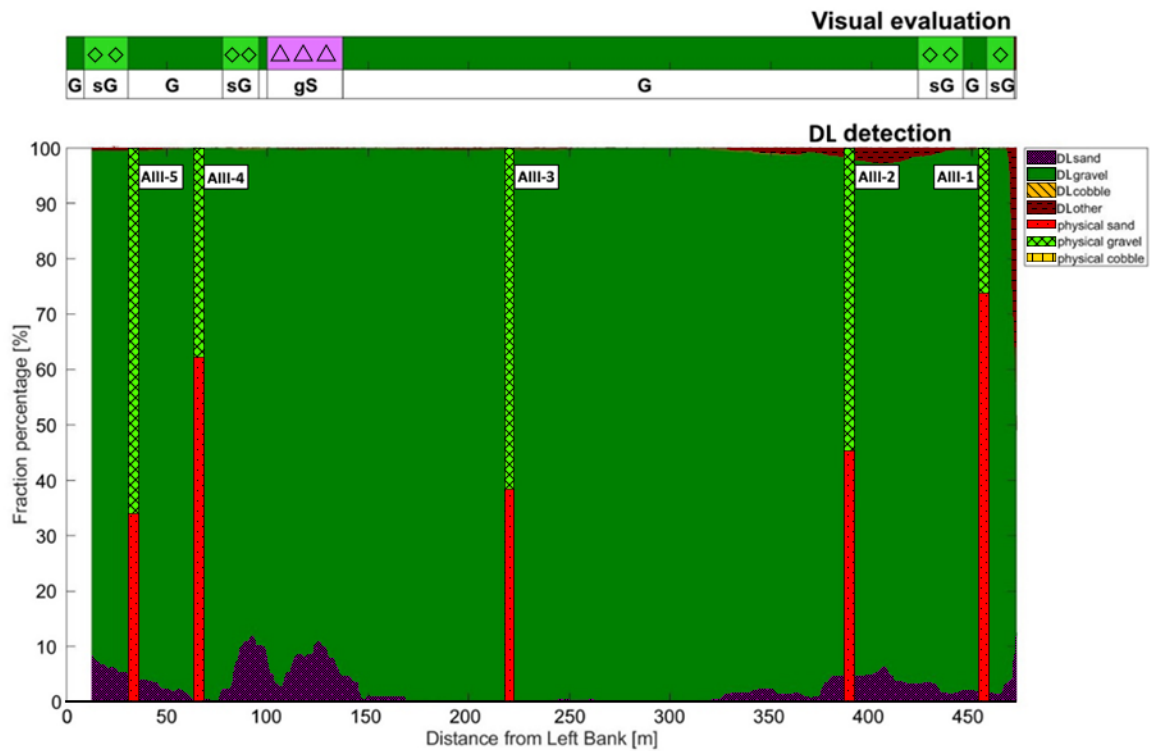
1213

Figure C5: Riverbed video images overlapped with their raw, DL detection result, at the sampling points in Section A-I.

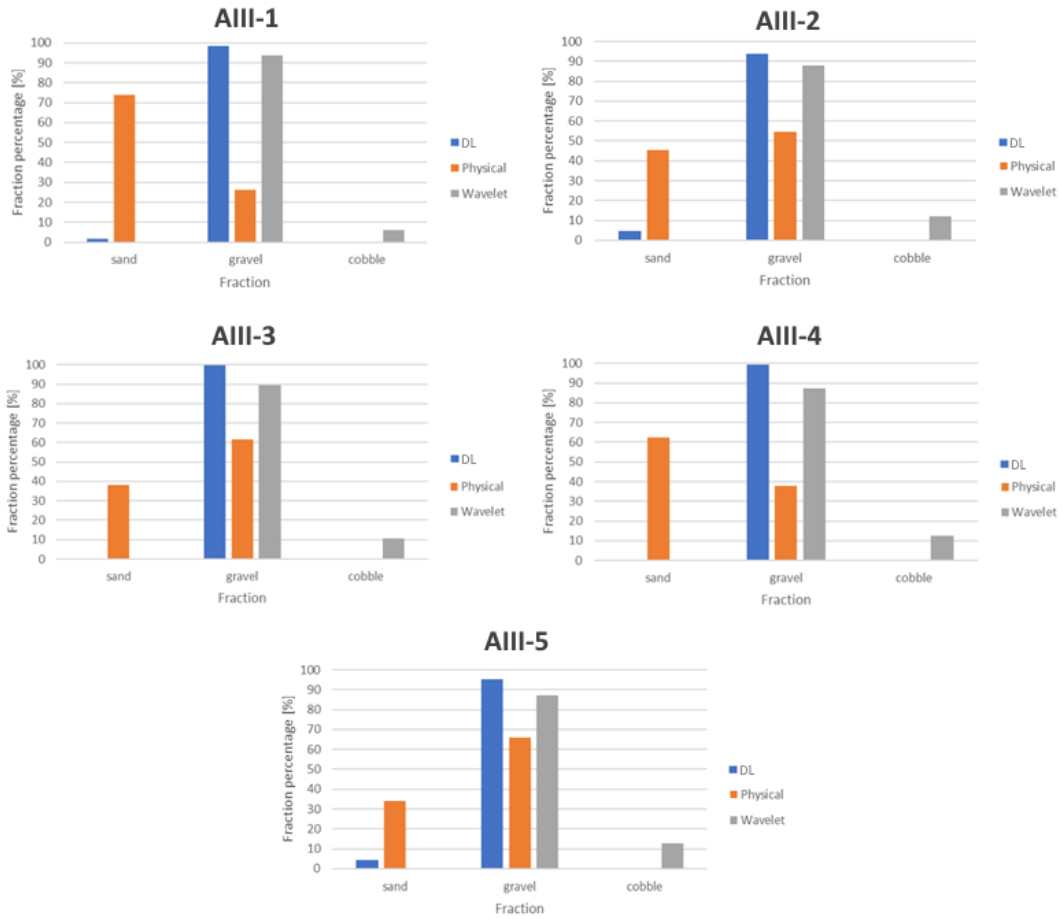


1215
1216 Figure D1: The path of the vessel and camera in Section A - III, Site A. The polyline is coloured based on the sediment
1217 seen during visual evaluation of the video. Yellow markers are the locations of physical bed material samplings. (Map
1218 created with Google Earth Pro)

1219

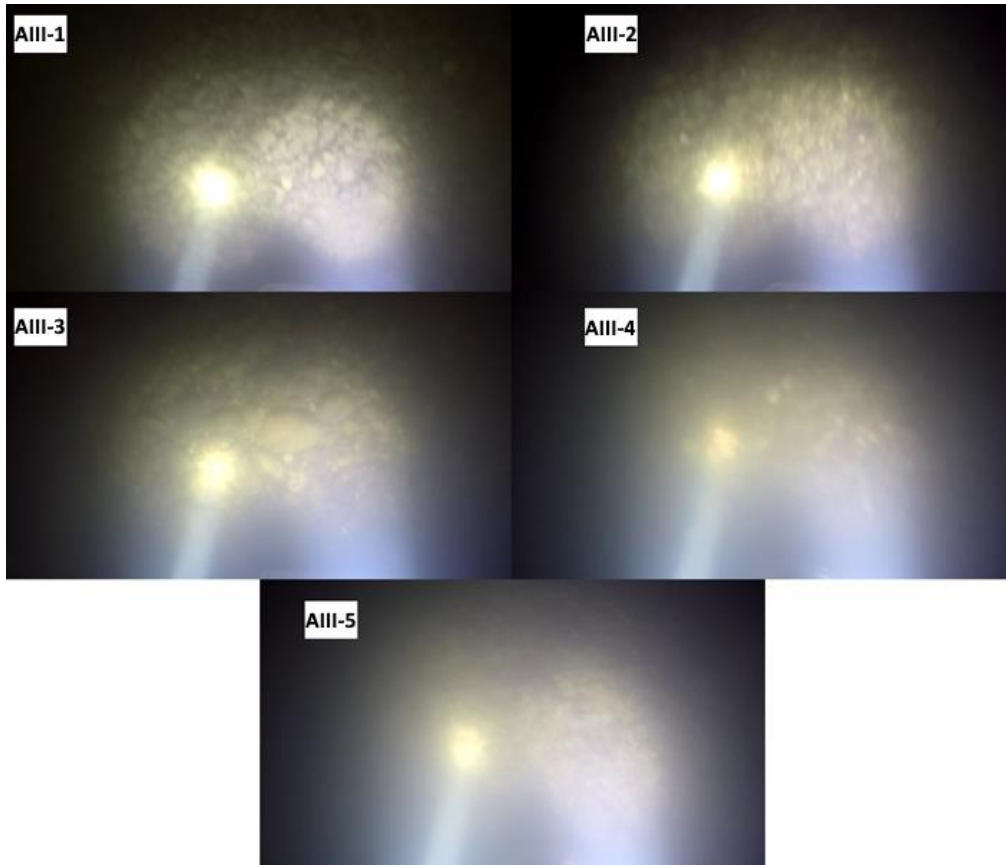


1220
1221 Figure D2: Sediment fraction percentages in Section A - III, recognised by the AI. The visual evaluation included three
1222 classes: gravel – G, sandy gravel – sG, gravelly sand - gS). The fractions of the physical samples are shown as verticals.



1223
1224
1225

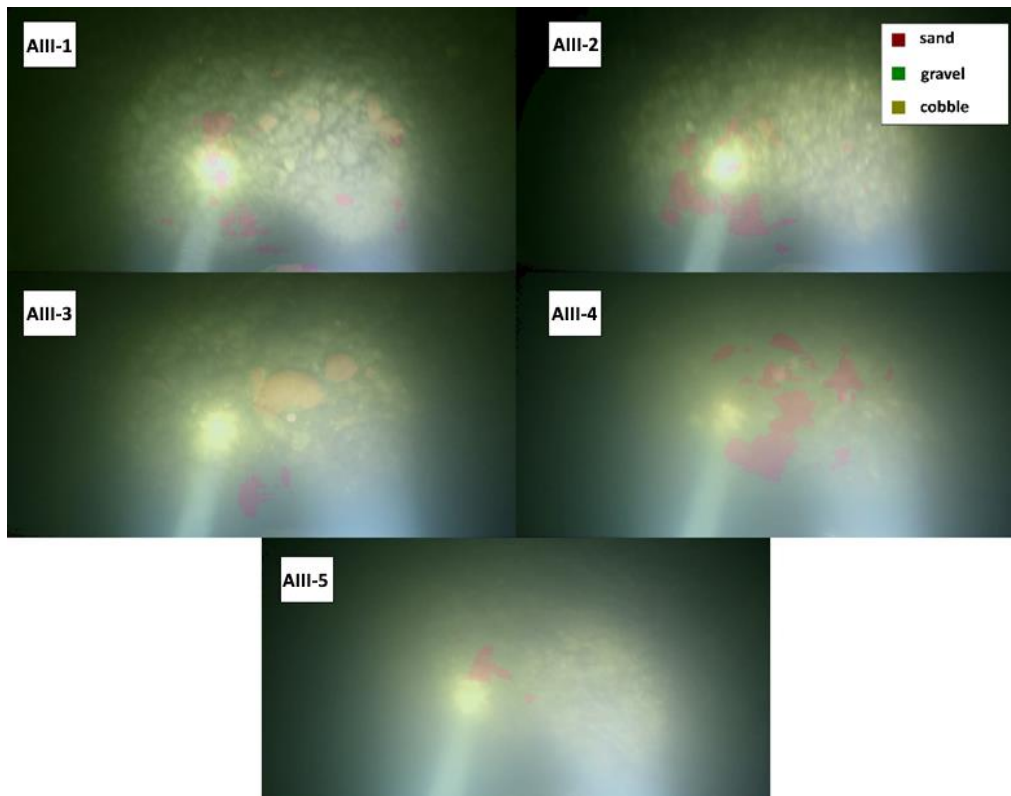
Figure D3: Comparison of sediment fraction % at the sampling locations from the moving-averaged DL detection, conventional sieving and the wavelet-based image processing method. Section A - III.



1226
1227

Figure D4: Riverbed video images at the sampling points in Section A - III.

1228

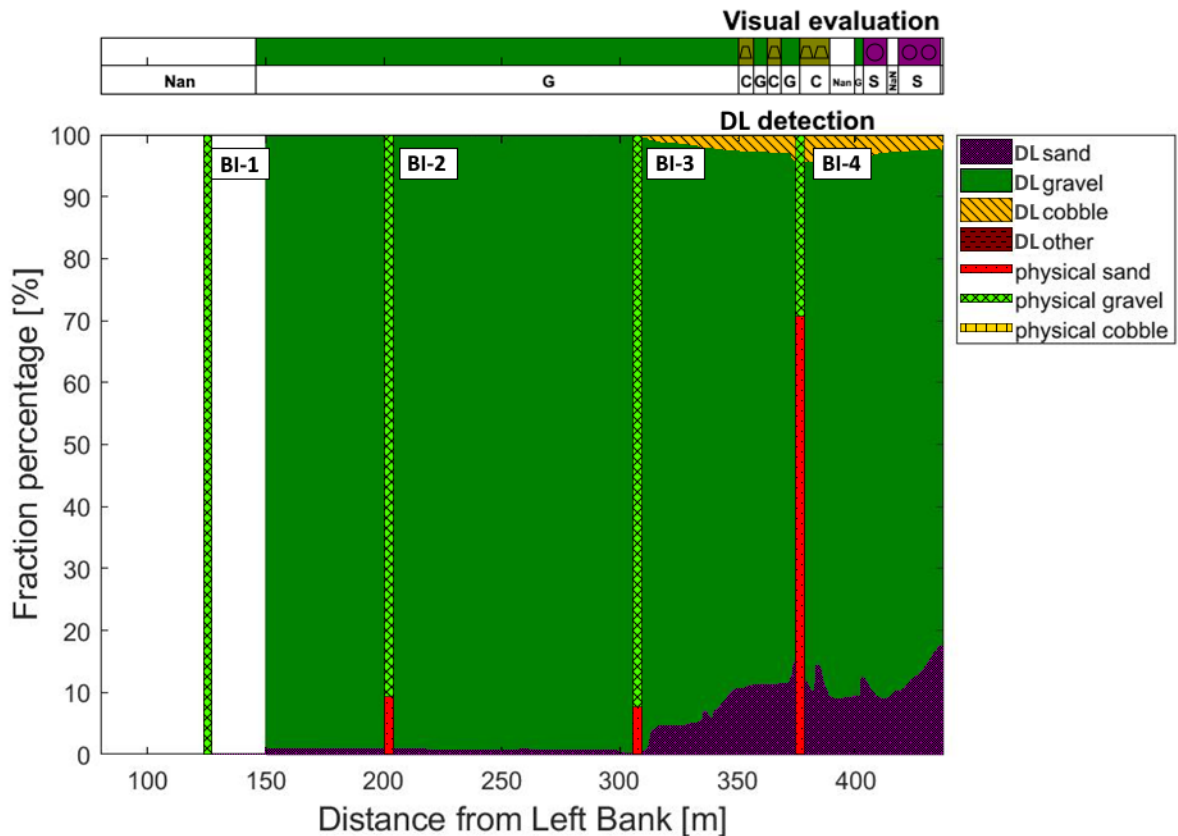


1229
1230
1231
1232

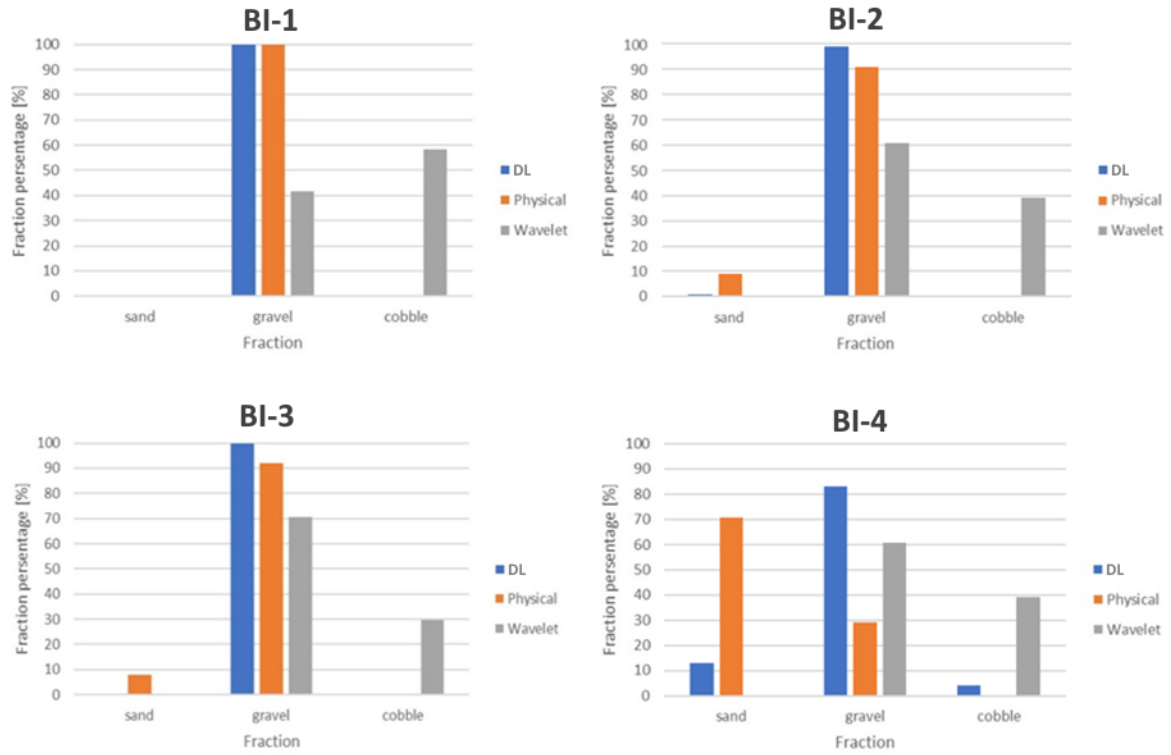
Figure D5: Riverbed video images overlapped with their raw, DL detection result, at the sampling points in Section A - III.



1234 Figure E1: The path of the vessel and camera in Section B - I, Site B. The polyline is coloured based on the sediment
 1235 seen during visual evaluation of the video. Yellow markers are the locations of physical bed material samplings. (Map
 1236 created with Google Earth Pro)
 1237

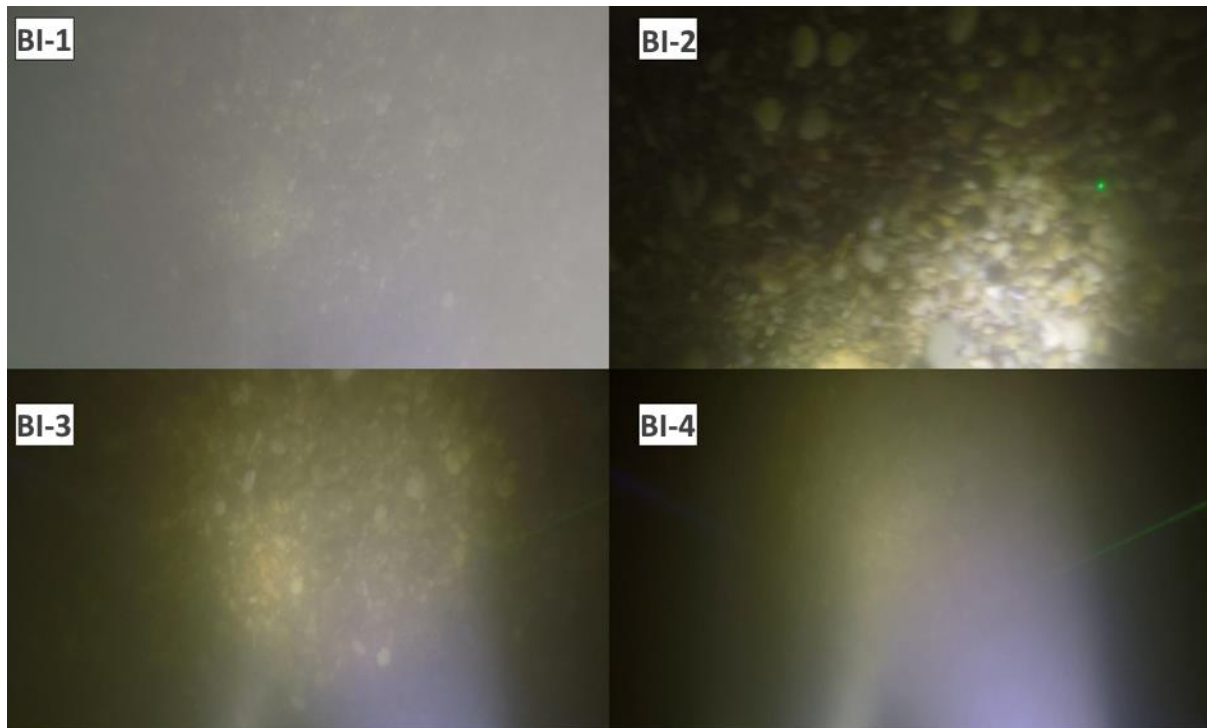


1238 Figure E2: Sediment fraction percentages in Section B - I, recognised by the AI. The visual evaluation included two
 1239 classes: gravel – G, sand – S). The fractions of the physical samples are shown as verticals.
 1240



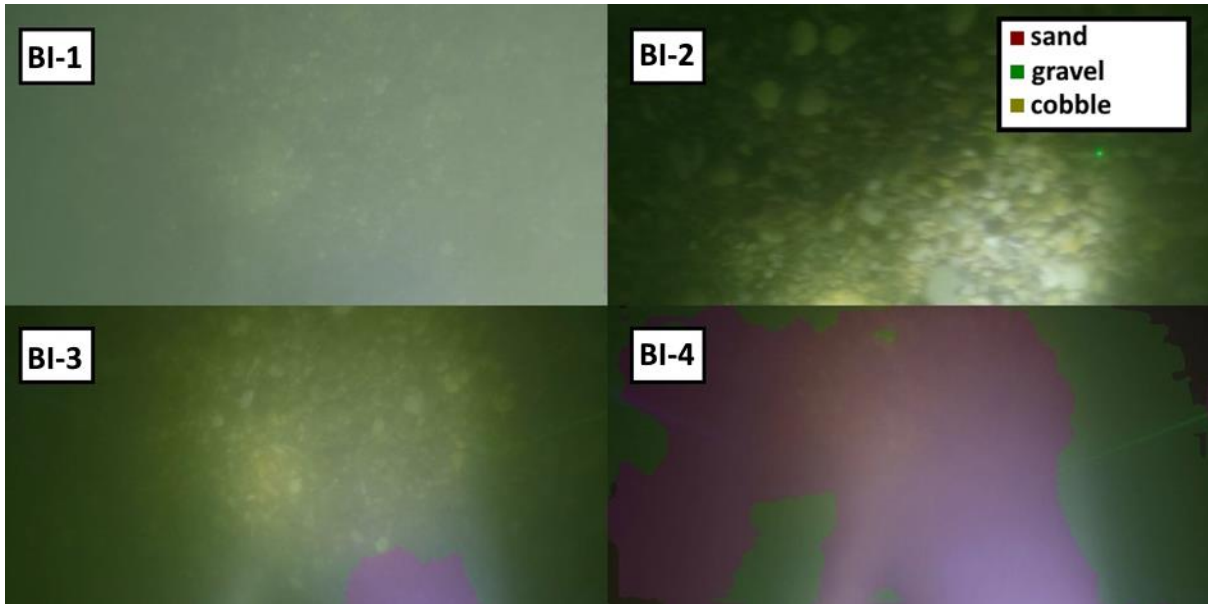
1241
1242
1243

Figure E3: Comparison of sediment fraction % at the sampling locations from the moving-averaged DL detection, conventional sieving and the wavelet-based image processing method. Section B - I.



1244
1245
1246

Figure E4: Riverbed video images at the sampling points in Section B - I.

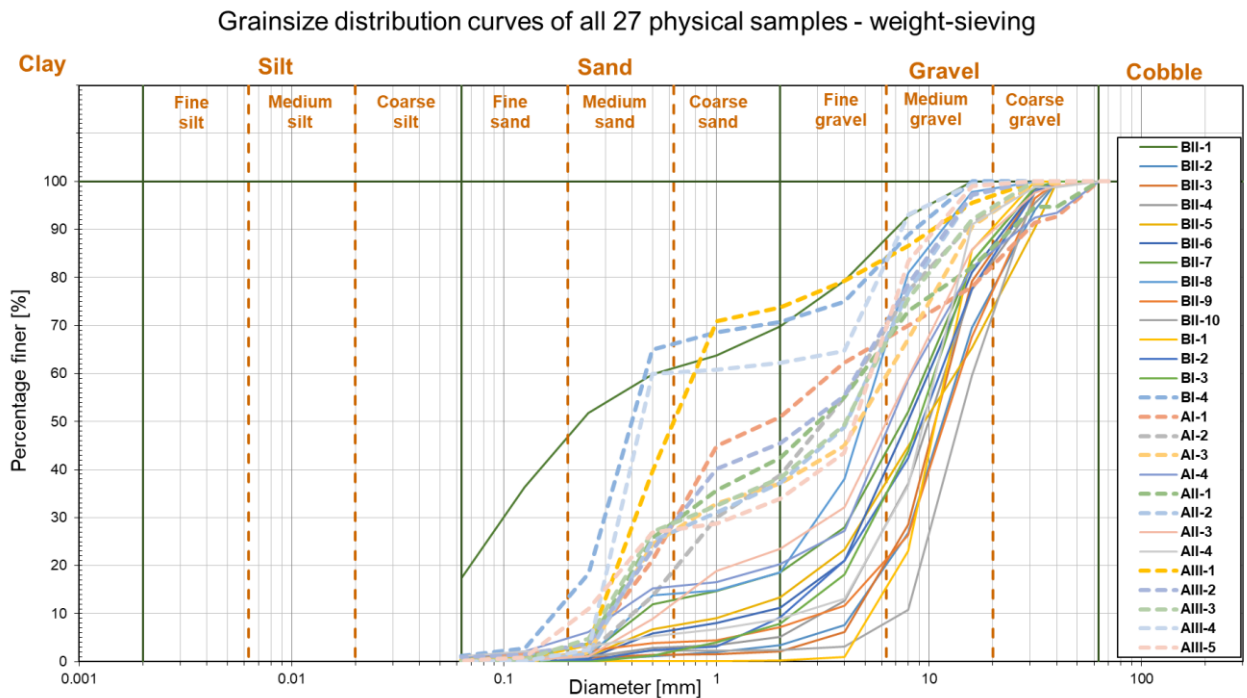


1247
1248
1249

Figure E5: Riverbed video images overlapped with their raw, DL detection result, at the sampling points in Section B - I.

1250

1251 Appendix F



1252
1253
1254
1255
1256
1257

Figure F1: Grainsize distribution curves of the 27 sieved physical samples. 11 curves categorised as Outlier Type-A are showcased with dashed lines. The shapes of these curves are representing bimodal (gap graded) sediment distributions, which typically refers to bed armouring (i.e., excess of a certain particle size, a coarser surface layer protects a finer subsurface layer from being washed away). Hence, analysing images of the surface layer could not represent these complex distributions inherently.